Contrib Mineral Petrol (2002) 144: 347–364
DOI 10.1007/s00410-002-0402-5

ORIGINAL PAPER

Julian R. Ballard · J. Michael Palin · Ian H. Campbell

Relative oxidation states of magmas inferred from Ce(IV)/Ce(III) in zircon: application to porphyry copper deposits of northern Chile

Received: 22 October 2001 / Accepted: 25 July 2002 / Published online: 8 October 2002

Abstract Major- and trace-element compositions of zircons and whole rocks from 14 barren and seven ore-bearing calc-alkaline intrusions from the Chuquicamata-El Abra porphyry copper belt of northern Chile have been measured in situ by excimer laser ablation (ELA) ICP-MS. These data permit the Ce(IV)/Ce(III) ratio within zircon to be calculated using a lattice-strain model for mineral-melt partitioning of Ce(IV) and Ce(III). Zircon Ce(IV)/Ce(III) and Eu_N/Eu_N^* ratios, and by inference magmatic oxidation states, generally increase from older, mafic to younger, felsic units. Within this sequence, porphyry copper mineralization is directly associated only with intrusions with zircon Ce(IV)/Ce(III) > 300 and $Eu_N/Eu_N^* > 0.4$. Such trends can be understood in terms of interdependent relations between oxygen fugacity, sulfur speciation and solubility, and chalcophile element partitioning in silicate magmas. Because zircon occurs in most calc-alkaline intrusions and is resistant to subsolidus alteration, zircon Ce(IV)/Ce(III) ratios provide a useful tool for evaluating the economic potential of such rocks for magmatic-hydrothermal $Cu \pm Au$ mineralization. The approach is general and may provide a means to infer relative oxidation state in a wide range of intermediate to felsic igneous rocks.

J.R. Ballard · J.M. Palin (✉) · I.H. Campbell
Research School of Earth Sciences,
Australian National University,
Canberra, ACT 0200, Australia
E-mail: michael.palin@stonebow.otago.ac.nz
Tel.: +64-3-4799083
Fax: +64-3-4797527

Present address: J.M. Palin
Department of Geology,
University of Otago, Dunedin 9001, New Zealand

Editorial responsibility: W. Collins

Introduction

Studies of magmatic-hydrothermal $Cu \pm Au$ deposits reveal a persistent spatial association with oxidized calc-alkaline intrusions (e.g., Candela 1992; Blevin and Chappell 1992; Hedenquist and Lowenstern 1994). This association suggests that a genetic link exists between oxidized magmas and processes leading to $Cu \pm Au$ mineralization, most likely involving redox control of the speciation and solubility of magmatic sulfur and its influence on the fractionation of chalcophile elements. From the perspective of mineral exploration, this association means that the oxidation state of intrusions could be used as an empirical criterion to distinguish between ore-bearing and barren magmatic-hydrothermal systems. It is, therefore, of considerable economic as well as scientific interest to determine the magmatic oxidation state of such intrusions. Unfortunately, quantitative oxygen barometers based on Fe–Ti oxides are prone to resetting during slow cooling of intrusive rocks, and empirical redox indicators such as the whole-rock Fe(III)/Fe(II) ratio or the presence of anhydrite rarely survive processes of hydrothermal alteration and surficial weathering. Here, we present a method of determining the Ce(IV)/Ce(III) ratio in zircon and use it to examine the temporal evolution of oxidation state in a suite of barren and ore-bearing intrusions. Zircon is well suited to this task, as it is a widespread accessory mineral in intermediate to felsic igneous rocks and is resistant to hydrothermal alteration and physical and chemical weathering. Zircon partitions Ce(IV) in strong preference to Ce(III), which means the Ce(IV)/Ce(III) ratio should be a sensitive and robust measure of magmatic oxidation state.

This study is based on the Los Picos-Fortuna/Pajonal-El Abra igneous complex, a suite of spatially and temporally associated calc-alkaline intrusions within the Chuquicamata-El Abra porphyry copper belt of northern Chile. The complex is cut by a major strike-slip fault, the West Fault, with the Pajonal-El Abra intrusive suite

displaced ca. 35 km to the north of the correlative Los Picos-Fortuna intrusive suite. The Los Picos-Fortuna/Pajonal-El Abra complex was emplaced over a period of about 5.5×10^6 years (Ballard et al. 2003) and shows a systematic compositional evolution with time through a sequence of barren intrusions, culminating in the ore-bearing El Abra porphyry. This igneous complex provides an ideal opportunity to examine the role of oxidation state in a magmatic system which eventually produced a porphyry copper deposit. The study is supplemented by analyses of zircons from other ore-bearing porphyries in the belt, including the super-giant Chuquicamata copper deposit, as well as the smaller Radomiro Tomic and Opache deposits, to establish whether there is a systematic difference between ore-bearing and barren intrusions.

Geological setting

Geology of the Chuquicamata-El Abra belt

The Chuquicamata-El Abra belt in northern Chile (Fig. 1) hosts several important porphyry copper deposits, including one of the world's largest, Chuquicamata. It forms part of a more extensive north-south-trending corridor of porphyry copper deposits of Eocene-Oligocene age which includes Collahuasi, Escondida and Potrerillios (Sillitoe 1992). The basement of the belt is composed of a variety of pre-Cenozoic igneous, sedimentary and metamorphic rocks. Calc-alkaline igneous activity dominated the late Cretaceous to Oligocene history of the Chuquicamata-El Abra belt, but only Eocene to Oligocene intrusive rocks host porphyry copper mineralization. The major mines and prospects include Chuquicamata, El Abra, Radomiro Tomic, Opache, and Mansa Mina (Sillitoe et al. 1996; Cuadra et al. 1997; Ossandón and Zentilli 1997; Pardo and Rivera 1999). Miocene to Holocene alluvial, colluvial and eolean sediments as well as some volcanic flows were deposited after emplacement of the porphyries and now mantle the greater part of the region (Boric et al. 1990; Maksaev et al. 1994; Maksaev and Tomlinson 1995; Tomlinson et al. 1995).

Since the Jurassic, regional compression associated with subduction of the Phoenix, Farallon and then Nazca plates (Duncan and Hargraves 1984) has been responsible for deformation along the western margin of South America. Changing patterns of stress have led to extensional, thrust and strike-slip faulting, as well as widespread folding. The West Fault zone is the major structure in the Chuquicamata-El Abra belt, forming part of the north-south-orientated Domeyko Fault System which extends for over 2,000 km in northern Chile (Lindsay et al. 1995; Reutter et al. 1996; Dilles et al. 1997; McInnes et al. 1999).

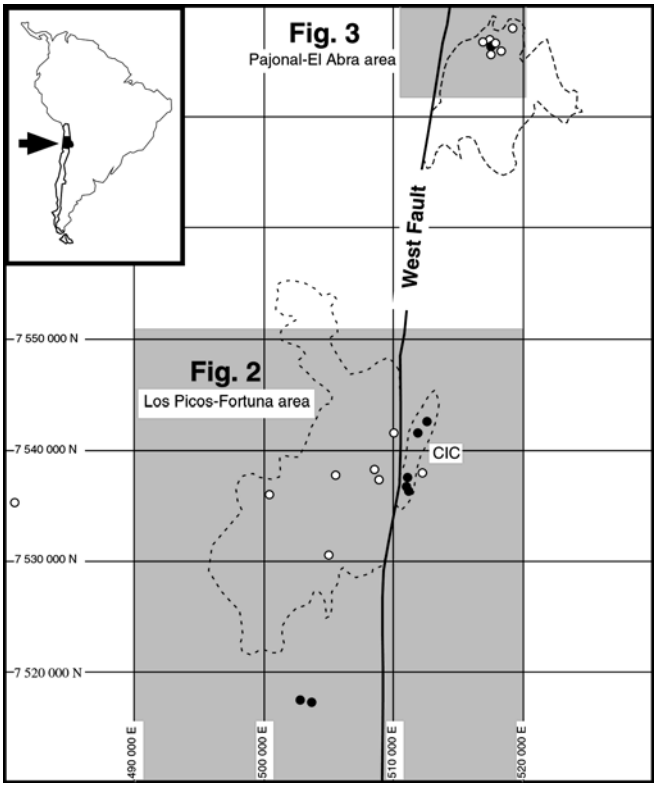

Fig. 1 Map of the Chuquicamata-El Abra porphyry copper belt in northern Chile (modified from Maksaev and Tomlinson 1995; Tomlinson et al. 1995; Reynolds et al. 1998; Pardo and Rivera 1999) showing the approximate outline of the Los Picos-Fortuna and Pajonal-El Abra igneous suites, the Chuquicamata Intrusive Complex, and the locations of igneous rock samples used for zircon trace-element analysis. *Open symbols* indicate barren units, and *closed symbols* are ore-bearing intrusions

Los Picos-Fortuna and Pajonal-El Abra igneous suites

The Los Picos-Fortuna igneous suite outcrops west of the Chuquicamata mine across the West Fault and consists of Los Picos quartz monzodiorite (Dilles et al. 1997) and the Fortuna intrusive complex (Fig. 2). Los Picos is thought to consist of multiple plutons, evidenced by monzonitic bodies intruding diorites (Rosas 1999). It outcrops as a north-south-trending belt along the western extremity of the Fortuna complex, and as isolated roof pendants within these intrusions. The Fortuna complex intrudes Los Picos along its eastern and northern margins, forming a continuous linear outcrop approximately 20 km (north–south) by 5 km (east–west). It is composed of Gris granodiorite and monzonite, Clara hornblende granodiorite, small leucocratic intrusions, and the San Lorenzo rhyodacite porphyry (Rosas 1999). Broadly, the Fortuna complex becomes younger from west (Gris) to east (Clara; Rosas 1999).

Forty-five kilometers north of the Chuquicamata mine and 2 km east of the West Fault, the El Abra complex intrudes upper Carboniferous to middle Triassic plutonic and volcanic rocks and Cretaceous continental sediments (Boric et al. 1990; Tomlinson et al. 1995; Maksaev and Tomlinson 1995; Fig. 3).

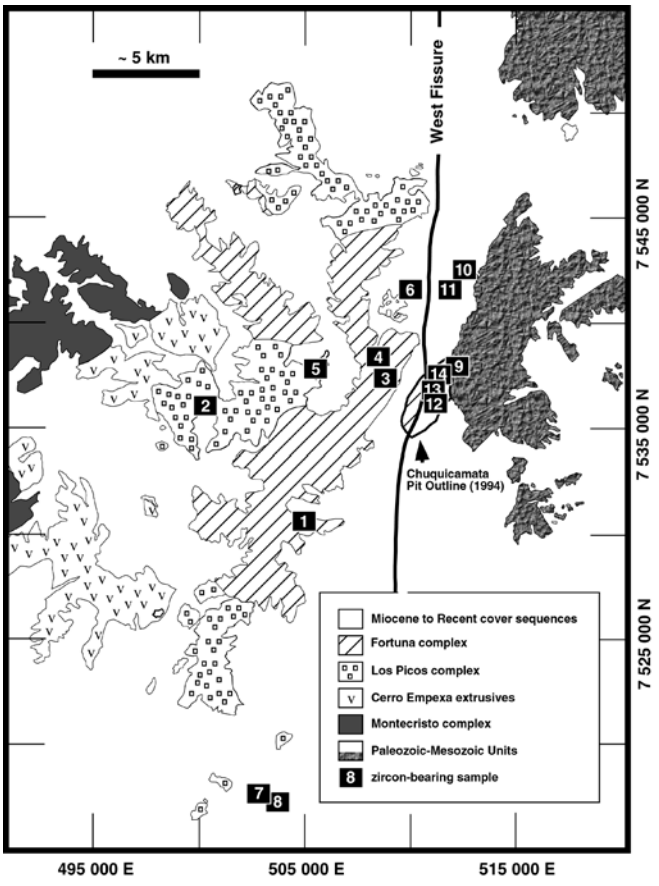

Fig. 2 Geologic map of the Chuquicamata mine and surrounding area (modified from Chong and Pardo 1994). Locations and identities of samples are as follows: *1* and *2* Los Picos monzodiorite, *3* Gris granodiorite, *4* Clara granodiorite, *5* San Lorenzo rhyodacite porphyry, *6* leucocratic intrusive, *7* and *8* Opache mine porphyry, *9* Elena granodiorite, *10* Radomiro Tomic major facies porphyry and *11* minor facies porphyry. Samples of East (*12*), West (*13*) and Bench (*14*) porphyries come from within the Chuquicamata mine

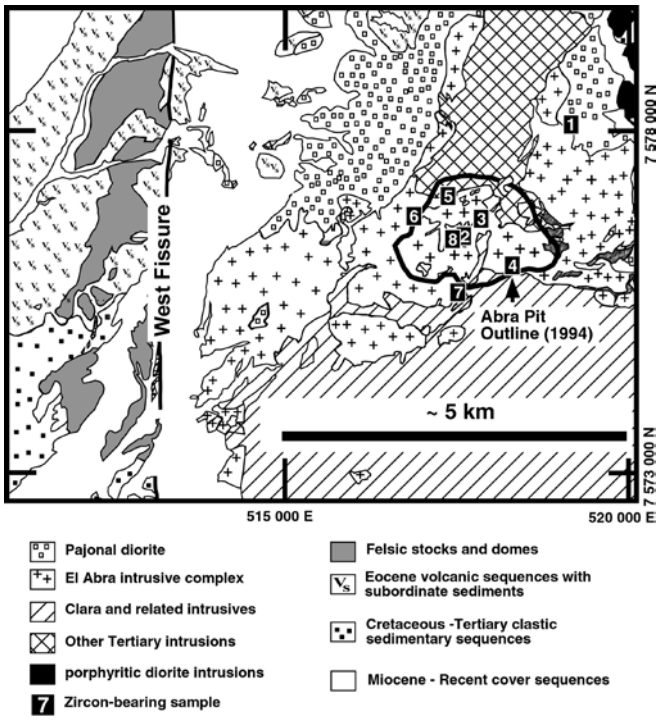

Fig. 3 Geologic map of the El Abra area (modified from Tomlinson et al. 1995, and Graichen et al. 1995). Locations of samples are as follows: *1* Pajonal diorite, *2* Apolo leucogranite, *3* Dark diorite, *4* Central diorite, *5* El Abra aplite, *6* Equis monzodiorite, *7* South granodiorite, and *8* El Abra mine porphyry

The northern extent of the El Abra complex is defined by a sharp contact made with older Pajonal diorite (Dilles et al. 1997). Together, these comprise the Pajonal-El Abra igneous suite. The El Abra complex consists of quartz and biotite diorites (Dark and Central diorite), Equis monzodiorite, South granodiorite, El Abra quartz monzonite porphyry, Apolo alkali biotite leucogranite, aplite, and undifferentiated intrusive breccia (Graichen et al. 1995). Diorite and porphyry host the bulk of the ore within the El Abra mine (Ambrus 1977; Maksaev et al. 1994), although the source of the copper has not been proven.

Based on previous geological mapping, structural reconstructions, and geochemical data (Graichen et al. 1995; Dilles et al. 1997; Rosas 1999), the Los Picos-Fortuna and Pajonal-El Abra igneous suites are interpreted to have formed part of a contiguous batholith prior to net sinistral displacement along the West Fault. Our recent zircon geochronology and geochemical analysis confirm this interpretation and indicate that this composite body was emplaced over 5.5×10^6 years between 42.9 and 37.4 Ma (Ballard et al. 2003). In addition, the zircon geochronology allows the emplacement sequence of the individual plutons of the Los Picos-Fortuna/Pajonal-El Abra complex to be established, and shows that the compositionally evolved and ore-bearing El Abra porphyry is the youngest unit. The spatial association of a significant copper deposit with the youngest porphyry suggests a genetic link between magmatic-hydrothermal mineralization and the final stages of the magmatic evolution of this large igneous complex.

Other Eocene porphyry copper deposits

Immediately east of the Fortuna intrusive complex, the super-giant Chuquicamata copper deposit (Fig. 2) lies at the southern end of the 14 by 2 km, north-south-trending Chuquicamata Igneous Complex (CIC; Zentilli et al. 1994; Tomlinson et al. 1995; Maksaev and Tomlinson 1995; Pardo and Rivera 1999). In the Chuquicamata mine, the CIC consists of three intrusions, the East, West and Bench porphyries, which can be distinguished on the basis of texture and varying proportions of plagioclase, quartz, orthoclase and biotite phenocrysts (Aracena 1981). The Radomiro Tomic copper deposit is located 7 km north of the Chuquicamata mine, also within the CIC (Cuadra et al. 1997). At Radomiro

Tomic, copper mineralization is hosted within two distinct porphyry intrusions which are texturally very similar to the Chuquicamata porphyries.

The Opache prospect is located 6 km west of the West Fissure, about 20 km south-southwest of Chuquicamata (Fig. 2). Preliminary work suggests that Opache mineralization consists of hydrothermal breccias which cross cut a series of hypabyssal dacite and tonalite porphyries which intrude andesite volcanics (Williams 1997). Basement in this part of the district is thought to consist of Paleozoic to Cretaceous metamorphic rocks, which is supported by their inclusion as clasts in some hydrothermal breccia samples (Williams 1997). A limestone sequence covers the Opache prospect, locally reaching a thickness of over 200 m (Pardo and Rivera 1999).

Indicators of magmatic oxidation state

Aerially extensive hydrothermal alteration has destroyed many of the primary mineralogic and chemical indicators of oxidation state in igneous rocks of the Chuquicamata-El Abra porphyry copper belt. Iron–titanium oxides are rarely preserved, primary mafic phases are widely replaced by chlorite, and most biotite is Mg-rich and probably of hydrothermal origin. An exception is Los Picos diorite in which exsolved hematite–ilmenite coexists with Ti-poor magnetite and Mg-rich biotite. Based on reconstructed hemo-ilmenite compositions and assuming a cystallization temperature of ca. 900 °C, the estimated oxygen fugacities for this unit lie about one log unit above FMQ (fayalite–magnetite–quartz), using the calibration of Anderson et al. (1993).

Methods

Zircon trace-element analysis

Zircons were separated by standard magnetic and density methods (Allen et al. 1998) from 2-kg samples collected from drill core and outcrop (Figs. 1, 2, 3). The separated grains were mounted in epoxy and polished to expose their centers. Using a combination of cathodoluminescence and optical microscopy, the clearest, least fractured rims of the zircon crystals were selected as suitable targets for laser ablation.

Sample mounts were placed in a custom-designed sample cell flushed with Ar and He (Loucks et al. 1995; Eggins et al. 1998). Laser ablation was accomplished using a pulsed Lambda Physik LPX 120I UV ArF excimer laser operated at a constant voltage (between 21 and 23 kV) at 5 Hz, with a spot diameter of 29 μm. The ablated material was carried by the He–Ar gas via a custom-made flow homogenizer to the ICP-MS. Raw count rates for the indicated isotopes were recorded in time-resolved mode, peak hopping in pulse counting mode. Data were acquired for 20 s with the laser off, and 40 s with the laser on, giving approximately 120 mass scans for a penetration depth of ca. 20 μm. Each block of eight unknowns was bracketed by analysis of a standard and took approximately 20 min. Data were acquired during three separate analytical sessions. The first employed a Perkin-Elmer ELAN 6000 ICP-MS, whereas the final two sessions used an Aligent 7500 ICP-MS. Four samples were repeated to ensure that both instruments produced consistent analytical results. Fused whole-rock glasses were analyzed in an identical way to the zircons.

Raw elemental count rates were converted to concentrations (in parts per million) offline using a spreadsheet on a PC. Corrections were made for mass bias drift which was evaluated by reference to standard glass NIST 612 (Pearce et al. 1997). After triggering, it took three to four mass scans for the count rates to reach a steady state, so these initial data were excluded from the calculations. Trace-element concentrations were obtained by normalizing count rates for each analyzed element to those for Si, and assuming SiO_2 to be stoichiometric in zircon with a concentration of ca. 32.8 wt%.

The laser ablation spots in zircon are carefully selected to avoid mineral and glass inclusions, inherited cores, and cracks, and most grains displayed smooth elemental patterns. However, it is difficult to avoid all subsurface heterogeneities. Apatite is a common inclusion in zircon which can strongly perturb LREE concentrations in zircon. To monitor for apatite inclusions, phosphorus was included in the list of elements measured. Zircons with high P count rates almost always displayed correspondingly high levels of LREEs, usually within discrete depth intervals (Fig. 4), consistent with the apatite inclusion hypothesis. These data intervals were excluded from the calculations.

Whole-rock trace element analysis

Whole-rock powders were mixed with a thulium-spiked lithium metaborate flux, fused at 1,200 °C, and quenched to produce a homogeneous glass beads. Glass chips were set in an epoxy mount and the ELA-ICP-MS analyses followed a similar approach to zircon analysis. Whole-rock glasses were ablated using a spot diameter of 103 μm, background data were acquired for 30 s with the laser off, and trace-element data were acquired for 60 s with the laser on. This gave a total of approximately 180 mass scans for a penetration depth of ca. 30 μm. Whole-rock trace-element concentrations were obtained by normalizing counts for each analyzed element to the doped Tm concentration of ca. 27 ppm. These were checked against XRF-based CaO compositions in sample replicates and well-documented standards.

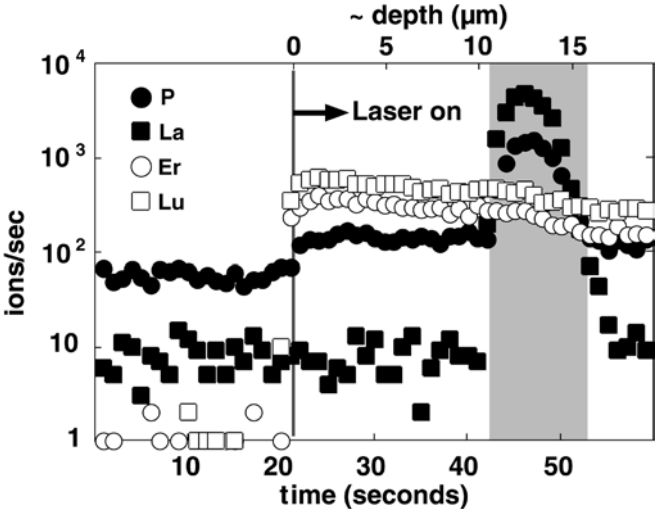

Fig. 4 Raw signal intensities (ions/s) for ^{31}P, ^{139}La, ^{166}Er and ^{175}Lu obtained from ELA-ICP-MS analysis of a zircon from the El Abra complex. The rapid rise and fall of the ^{31}P and ^{39}La count rates in the *shaded interval* (42–52 s, 11–16 μm depth), with no effect on the HREE counts, is interpreted to be due to an inclusion of LREE-enriched apatite. Such data intervals are excluded from the Ce(IV)/Ce(III) calculations described in the text

Theory

Zircon ($ZrSiO_4$) is a common accessory mineral in igneous rocks of intermediate to felsic composition. Tetravalent cations of appropriate size such as Hf, Th, and U readily substitute for Zr, as do the trivalent heavy rare-earth elements (HREEs), although the exact mechanism of charge compensation is uncertain (Hanchar et al. 2001). By contrast, the light rare-earth elements (LREEs) are strongly excluded by zircon, except for Ce which usually exhibits a chondrite-normalized concentration higher than those of the adjacent LREEs, La and Pr (Fig. 5). Such a positive Ce anomaly is unique among igneous minerals and indicates that Ce(IV) is partitioned into zircon in strong preference to Ce(III) because of its identical charge and similar size in eight-fold coordination (0.97 Å) to Zr (r = 0.84 Å). By similar reasoning, Eu(III) should be incorporated preferentially into zircon relative to Eu(II), although in this case the redox signal may be complicated by the effects of plagioclase crystallization.

In order to use the Ce anomaly in zircon as a measure of oxidation state, the Ce(IV)/Ce(III) ratio must be determined. Spectroscopic methods are inappropriate because Ce is present at trace concentration levels in zircon (e.g., ppm levels) and valence states are unlikely to be retained subsequent to crystallization. Instead, we employ an indirect approach described by Philpotts (1970) for determining the Eu(III)/Eu(II) ratio in plagioclase based on chemical analysis of two equilibrated phases modified for the case of Ce(IV) and Ce(III) in zircon. The total concentrations of Ce in zircon and coexisting melt can be considered as sums of Ce(IV) and Ce(III) in each phase:

$$Ce_{zircon} = Ce(III)_{zircon} + Ce(IV)_{zircon} \quad (1)$$

$$Ce_{melt} = Ce(III)_{melt} + Ce(IV)_{melt} \quad (2)$$

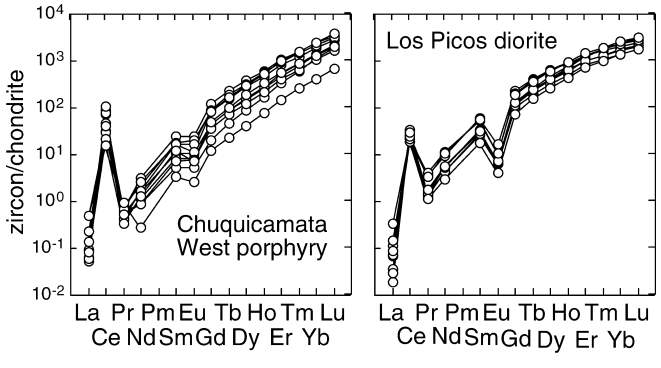

Fig. 5 Chondrite-normalized REE patterns for zircon from the Chuquicamata West porphyry (sample 98-609) and the Los Picos diorite (sample 98-521). Note the larger (more positive) Ce anomaly and smaller (less negative) Eu anomaly displayed by zircons of the West porphyry compared to those of the Los Picos diorite

By introducing separate distribution coefficients for Ce(IV) and Ce(III), these two equations can be combined to give:

$$Ce_{melt} = \frac{(Ce_{zircon} - Ce(IV)_{zircon})}{D^{zircon/melt}_{Ce(III)}} + \frac{Ce(IV)_{zircon}}{D^{zircon/melt}_{Ce(IV)}} \quad (3)$$

which upon rearrangement yields:

$$Ce(IV)_{zircon} = \frac{Ce_{melt} - \frac{1}{D^{zircon/rock}_{Ce(III)}} Ce_{zircon}}{\frac{1}{D^{zircon/rock}_{Ce(IV)}} - \frac{1}{D^{zircon/rock}_{Ce(III)}}} \quad (4)$$

Substituting Eq. (4) into Eq. (1) and solving for the concentration of Ce(III) in zircon gives:

$$Ce(III)_{zircon} = Ce_{zircon} - \frac{Ce_{melt} - \frac{1}{D^{zircon/rock}_{Ce(III)}} Ce_{zircon}}{\frac{1}{D^{zircon/rock}_{Ce(IV)}} - \frac{1}{D^{zircon/rock}_{Ce(III)}}} \quad (5)$$

Equations (4) and (5) can then be combined, rearranged and simplified to produce the following expression for the Ce(IV)/Ce(III) ratio in zircon:

$$(Ce(IV)/Ce(III))_{zircon} = \frac{Ce_{melt} - \frac{Ce_{zircon}}{D^{zircon/melt}_{Ce(III)}}}{\frac{Ce_{zircon}}{D^{zircon/melt}_{Ce(IV)}} - Ce_{melt}} \quad (6)$$

The analogous expression for the Eu(III)/Eu(II) ratio in zircon is:

$$(Eu(III)/Eu(II))_{zircon} = \frac{Eu_{melt} - \frac{Eu_{zircon}}{D^{zircon/melt}_{Eu(II)}}}{\frac{Eu_{zircon}}{D^{zircon/melt}_{Eu(III)}} - Eu_{melt}} \quad (7)$$

To solve Eq. (6) for the Ce(IV)/Ce(III) ratio in zircon, four values are needed: concentrations of Ce in zircon and melt, and zircon-melt distribution coefficients for Ce(IV) and Ce(III). The first value is measured directly by in-situ chemical analysis of zircon using ELA-ICP-MS, the second value is assumed to be equivalent to the whole-rock (as a proxy for melt) concentration of Ce also measured by ELA-ICP-MS, and the partition coefficients for Ce(IV) and Ce(III) can be estimated on the basis of crystal chemical constraints on trace-element partitioning.

It has been known for sometime that when mineral-melt distribution coefficients for isovalent cations are plotted as a function of ionic radius, they form smooth, concave-down parabolic curves (Onuma et al. 1968; Fig. 6). The apex of each parabola in these so-called Onuma diagrams corresponds to the optimal size of the crystal site into which the cations substitute, and its curvature reflects the elasticity of the surrounding lattice. Blundy and Wood (1994) quantified this relation using a thermodynamically based model relating the mineral-melt distribution coefficient (D_i) for a cation to the lattice-strain energy (ΔDG) induced by its misfit into a given crystal site:

$$D_i = D_0 e^{-\Delta G/RT} \quad (8)$$

where D_0 is the hypothetical strain-free distribution coefficient for a cation of optimal radius, R is the gas

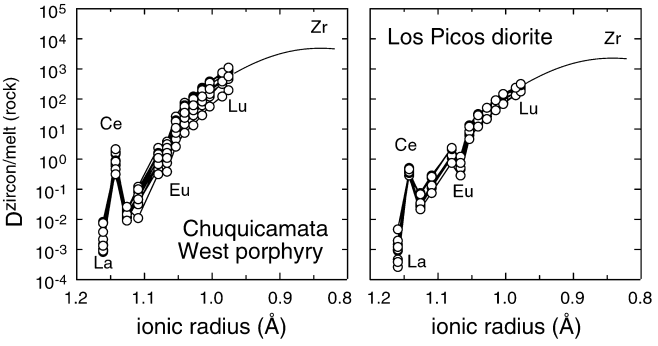

Fig. 6 Calculated distribution coefficients for REEs between individual zircons and average rock (as a melt proxy) for the Chuquicamata West porphyry and Los Picos diorite plotted versus ionic radii of the REEs as trivalent cations in eight-fold coordination. The curved trends form steep limbs of parabolic curves centered on the ionic radius of Zr (0.84 Å) which are characteristic of crystal chemically controlled trace-element partitioning (Onuma et al. 1968)

constant, and T is absolute temperature. The lattice-strain energy depends on the difference between the ionic radius of the cation (r_i) and the optimal site radius (r_0) through the Young's modulus (E) of the host crystal:

$$\Delta G = 4\pi E N_A \left[\frac{r_0}{2}(r_i - r_0)^2 + \frac{1}{3}(r_i - r_0)^3\right] \quad (9)$$

where N_A = Avogadro's number. Although the lattice-strain model may not explain all partitioning behavior (e.g., Ghaderi et al. 1999; Klein et al. 2000), it captures the first-order features, especially for structurally and compositionally simple minerals such as zircon.

Combining Eqs. (8) and (9), rearranging and taking logarithms yields a linear relation between mineral-melt distribution coefficients for a series of isovalent elements and a lattice-strain term involving their ionic radii:

$$\ln D_i = \ln D_0 - \frac{4\pi E N_A}{RT}\left(\frac{r_i}{3} + \frac{r_0}{6}\right)(r_i - r_0)^2 \quad (10)$$

When plotted according to Eq. (10) and assuming $r_0 = 0.84$ Å for Zr in eight-fold coordination, zircon-melt (or rock as a proxy for melt) distribution coefficients for tetravalent and trivalent cations form linear arrays (Fig. 7). These straight lines correspond to parabolas in an Onuma diagram. Because Ce and Eu are present as mixtures of Ce(IV) and Ce(III) and Eu(III) and Eu(II) in terrestrial magmas, the distribution coefficients for bulk Ce and Eu will fall somewhere between the tetravalent and trivalent and trivalent and divalent trends, respectively (Fig. 7). If all Ce were present in zircon as Ce(III), it would plot on the line defined by the trivalent REEs. Conversely, if all the Ce was Ce(IV), it would fall on the tetravalent line along with Zr, Hf, U(IV) and Th. By fitting a line to the trivalent REE array, a value for $D^{zircon/melt}_{Ce(III)}$ can be estimated. A similar procedure can be applied to the tetravalent (Zr–Hf–U–Th) trend to estimate $D^{zircon/melt}_{Ce(IV)}$. The resulting distribution coefficients for Ce(IV) and Ce(III) can be substituted into Eq. (6) and used in the calculation of the Ce(IV)/Ce(III) ratio in zircon. Because of the extremely slow diffusivities of trivalent and

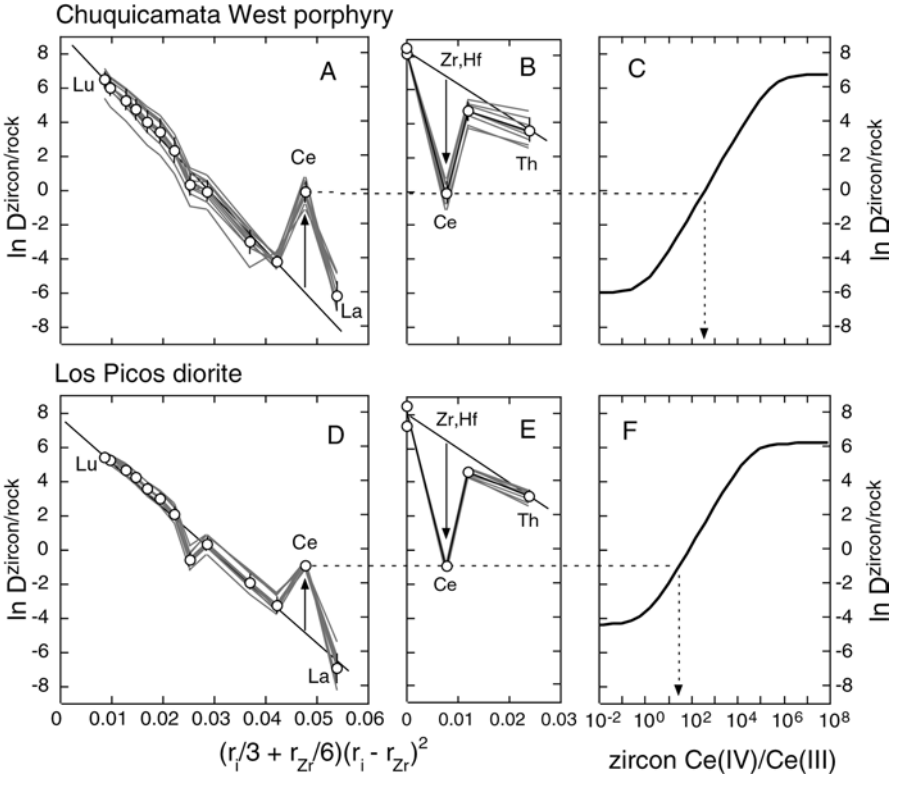

Fig. 7A–F Natural logarithm of zircon/rock distribution coefficients for the Chuquicamata West porphyry and Los Picos diorite plotted versus a lattice-strain parameter (modified from Blundy and Wood 1994) for trivalent (**A**, **D**) and tetravalent cations (**B**, **E**). As discussed in the text, linear arrays are predicted using these coordinates. Results from individual zircon grains are shown in *shading* and sample averages are shown in *bold* (with 1 standard deviation errors). Measured zircon/rock distribution coefficients for total Ce lie between those expected for Ce(III) and Ce(IV) based on the observed trends for trivalent and tetravalent cations, and can be used to calculate the Ce(IV)/Ce(III) ratio in zircon as illustrated (**C**, **F**). Note the high La value in **A** which is indicative of contamination by an LREE-enriched inclusion

tetravalent cations in zircon (Cherniak et al. 1997), such elemental characteristics should survive as long as the zircon crystal remains intact and thereby record the Ce(IV)/Ce(III) *at the time of crystallization*.

It is important to point out that zircon Ce(IV)/Ce(III) ratios greater than one do not imply the same for the parental melt. Zircon is the only common igneous mineral to exhibit a Ce anomaly and it does so as much because of an extreme discrimination against Ce(III) as a preference for Ce(IV). Hinton and Upton (1991) note that a positive Ce anomaly in zircon is consistent with crystallization from a melt with a Ce(IV)/Ce(III) ratio on the order of 10^{-3}. Melt Ce(IV)/Ce(III) ratios calculated using the zircon Ce(IV)/Ce(III) ratio and $D_{Ce(III)}^{zircon/melt}$ and $D_{Ce(IV)}^{zircon/melt}$ values determined for each sample of this study range from 0.5×10^{-3} to 1.2×10^{-3}. Mass-balance considerations indicate that fractional crystallization or accumulation of zircon are incapable of generating measurable Ce anomalies in magmas. Conversely, fractionation of LREE-enriched phases such as xenotime and monazite, although depleting residual melt in the LREEs, will not affect the calculation of Ce(IV)/Ce(III) ratios as described above because it is based on zircon-melt partitioning of REEs.

Results

Zircon trace-element data are presented in Tables 1 and 2 together with average whole-rock MgO, SiO_2, and trace-element data from Ballard et al. (unpublished data) and zircon U–Pb ages (Ballard et al. 2003). Calculated zircon Ce(IV)/Ce(III) and Eu_N/Eu_N^* ratios are also listed in Table 2 (where the subscript indicates chondrite normalization, and $Eu_N^* = (Sm_N \cdot Gd_N)^{1/2}$). In cases where zircon REE concentrations were close to the detection limit of the ICP-MS, no Ce(IV)/Ce(III) ratio has been calculated because of the large uncertainties involved. Individual grain and sample average zircon Ce(IV)/Ce(III) and Eu_N/Eu_N^* ratios are plotted versus host intrusion zircon U–Pb age in Fig. 8. We do not have an adequate explanation for the large range of ratios observed in zircons from individual samples. In several cases, outliers may represent inherited grains or portions of grains. It was not possible to simultaneously determine U–Pb ages and measure a full suite of trace elements in the same spot, so we cannot prove this was always the case. Nonetheless, older units have zircons with lower Ce(IV)/Ce(III) and Eu_N/Eu_N^* values than their younger counterparts, and these redox-sensitive ratios increase with decreasing emplacement age, with the notable exception of the leucocratic unit of the Fortuna complex. These data also show that the intrusions directly associated with porphyry copper deposits are characterized by having the highest zircon Ce(IV)/Ce(III) (>300) and Eu_N/Eu_N^* ratios (>0.4).

Discussion

Oxidation during magmatic differentiation

The major- and trace-element compositions of the Los Picos-Fortuna/Pajonal-El Abra igneous complex vary systematically with time (Ballard et al., unpublished data). This point is illustrated in Fig. 9, which shows that average MgO values of individual units within the complex decrease with age, although there is considerable range within units and overlap between units. Our preferred explanation for these data is that all intrusions were sourced from a single, large magma reservoir located deeper in the crust which was episodically replenished by mafic magma while undergoing progressive fractional crystallization and assimilation. We suggest that this deep, parental magma reservoir remained at least partially molten over the 5.5×10^6 year history of the complex. In this way, resident evolved melt could mix with injections of new mafic magma to form hybrid products which retained a chemical imprint of prior differentiation (Ballard et al., unpublished data). Importantly, the increase in the average Ce(IV)/Ce(III) ratios of zircon with time (Fig. 10) suggests that oxidation state also evolved progressively in the magma system. The Pajonal diorite represents the oldest, least oxidized stage of this evolution, and the ore-bearing El Abra mine porphyry is the youngest, most oxidized stage.

The other ore-bearing porphyries analyzed in this study, from Chuquicamata, Radomiro Tomic and Opache, do not have obvious precursor-barren intrusive sequences as does the Los Picos-Fortuna/Pajonal-El Abra complex. Nevertheless, the high Ce(IV)/Ce(III) ratios of the zircons from the ore-bearing units and their geochemical resemblance to the El Abra mine porphyry suggest that these intrusions may have experienced a similar magmatic evolution. It is therefore likely that the Chuquicamata, Radomiro Tomic and Opache porphyries are underlain by long-lived magma systems similar to that hypothesized for the Los Picos-Fortuna/Pajonal-El Abra complex.

The progressive increase in average zircon Ce(IV)/Ce(III) ratios in the Los Picos-Fortuna/Pajonal-El Abra complex is accompanied by a similar trend in average zircon Eu_N/Eu_N^* toward smaller (less "negative") Eu anomalies (Fig. 8D). These data are consistent with an increase in magmatic oxidation state and the Eu(III)/Eu(II) ratio over time if, as is expected on the basis of crystal chemical arguments given above, Eu(III) is partitioned preferentially into zircon relative to Eu(II). Such a hypothesis is supported by trends in whole-rock Eu_N/Eu_N^* from the complex. Because Eu(II) is compatible in plagioclase, with $D_{Eu}^{albite/melt} > D_{Eu}^{anorthite/melt} > 1$, fractional crystallization usually produces melts with pronounced, negative Eu anomalies, that is, $Eu_N/Eu_N^* < 1$ (Nash and Crecraft 1985; Bacon and Druitt 1988; Dunn and Sen 1994). However, Eu becomes

Table 1 Zircon and whole-rock trace-element data: age, SiO_2, MgO, P, Sr, Y, La, Ce, Pr, Nd, Sm, Eu, and Gd

Unit	Analysis[a]	Age (Ma)	±SE	SiO_2	±SD	MgO	±SD	P	Sr	Y	La	Ce	Pr	Nd	Sm	Eu	Gd
Pajonal-El Abra suite																	
Pajonal diorite	195-1							170	0.35	1,609	0.068	15	0.546	7.23	10.15	0.87	42.1
	195-10							196	0.36	1,735	0.074	15	0.532	6.95	10.38	0.95	47.4
	195-2							153	0.29	1,563	0.036	21	0.469	7.14	10.81	0.68	45.2
	195-4							153	0.31	1,545	0.062	20	0.574	7.82	11.32	0.82	46.1
	195-5							121	0.23	988	0.003	15	0.089	2.07	4.21	0.35	23.8
	195-6							149	0.37	1,596	0.068	21	0.623	8.55	11.33	0.69	45.9
	195-7							261	0.51	2,068	0.012	49	0.149	3.18	6.6	0.25	35
	195-8							177	0.37	1,809	0.105	18	0.646	8.51	11.92	0.73	48
	195-9							165	0.26	1,444	0.034	19	0.424	6.2	9.91	0.72	42.2
	Av. rock	42.9	0.5	62.71	3.39	2.35	0.93	857	330	23.35	31.9	69.1	7.96	30.6	5.84	0.952	4.81
Apolo leucog-ranite	174-1							140	0.26	1,056	0.044	11	0.403	5.53	7.11	1.17	29.8
	174-10							107	0.14	469	0.005	8	0.035	0.74	1.83	0.36	9.8
	174-2							123	0.21	795	0.055	10	0.312	4.55	6.51	0.8	24.2
	174-3							128	0.17	610	b.d.l.	10	0.09	1.37	2.63	0.47	14
	174-4							106	0.17	386	0.011	7	0.027	0.73	1.7	0.27	8
	174-5							111	0.15	413	0.007	9	0.042	0.56	1.75	0.26	8
	174-6							64	0.21	322	0.007	8	0.025	0.75	1.65	0.28	7.2
	174-7							98	0.14	384	0.004	9	0.028	0.64	1.23	0.18	7.3
	174-8							109	0.21	429	b.d.l.	9	0.019	0.76	1.9	0.32	9.5
	174-9							95	0.18	423	0.003	9	0.035	0.52	1.42	0.2	8.8
	Av. rock	41.3	0.4	70.92	1.21	1.07	0.06	386	226	12.61	20.8	44.6	4.88	17.8	3.16	0.59	2.45
Central diorite	131-1							212	0.22	905	0.018	15	0.182	2.41	4.04	0.7	20.5
	131-10							144	0.2	619	0.012	12	0.047	1.04	2.23	0.44	12.9
	131-3							205	0.42	2,067	0.072	18	0.443	6.61	9.92	1.66	48.3
	131-4							164	0.28	900	b.d.l.	14	0.093	1.83	3.27	0.69	18.1
	131-6							136	0.2	853	0.005	12	0.12	2.2	4.7	0.84	21.7
	131-7							173	0.17	580	0.005	9	0.085	1.52	3.05	0.51	14.4
	131-8							238	0.39	1,724	0.032	21	0.344	4.97	8.76	1.29	41.4
	131-9							164	0.22	746	0.007	12	0.117	1.87	3.11	0.62	16.1
	Av. rock	40.6	0.3	64.11	3.09	2.53	0.65	940	375	18.27	27.6	58	6.56	25.1	4.72	0.936	3.86
Dark diorite	180-1							236	0.34	1,507	0.013	53	0.176	2.88	5.63	1.21	30.9
	180-10							176	0.71	2,021	0.016	40	0.139	2.94	6.61	1.26	34.8
	180-2							313	0.63	3,423	0.097	41	0.565	9.75	19.65	5.37	96.4
	180-3							201	0.38	1,394	0.017	25	0.163	2.6	5.89	1.69	32.3
	180-4							327	0.72	3,952	0.073	46	0.649	11.26	21.57	6.41	108
	180-5							189	0.42	1,774	0.033	22	0.324	4.8	9.21	2.64	44.6
	180-6							195	0.44	1,835	0.058	23	0.205	3.23	6.64	1.54	31.7
	180-7							295	0.57	2,889	0.052	39	0.475	7.73	15.3	4.39	74.8
	180-8							191	0.5	2,326	0.024	27	0.319	6.31	11.89	3.06	58.1
	180-9							176	0.41	1,889	0.026	22	0.308	5.62	10.4	3.08	48
	Av. rock	40.2	0.5	58.16	4.72	3.88	1.32	1,017	726	14.3	21	41.9	4.85	19.5	3.84	0.96	3.21
Aplite	121-1							126	0.19	592	b.d.l.	11	0.062	1.37	3.07	0.77	15.1
	121-10							107	0.13	349	b.d.l.	11	0.021	0.38	1.32	0.26	6.8
	121-2							123	0.4	470	0.011	14	0.035	0.59	1.85	0.34	9.9
	121-3							152	0.17	602	0.001	13	0.053	1.07	2.4	0.51	13.6
	121-4							130	0.14	428	b.d.l.	13	0.037	0.58	1.65	0.38	9.7
	121-5							128	0.21	575	b.d.l.	15	0.009	0.53	1.43	0.36	9.7
	121-6							184	0.29	1,197	0.035	17	0.359	4.93	7.23	1.51	29.5
	121-7							104	0.15	333	0	9	0.028	0.51	1.26	0.26	6.9
	121-8							129	0.18	592	0.008	14	0.072	1.77	3.13	0.57	15.3
	121-9							141	0.19	565	0.004	16	0.058	0.87	2.23	0.48	12.5
	Av. rock	38.5	0.4	71.96	1.68	0.86	0.22	249	239	20.3	28.6	63.7	7.18	26.7	5.02	0.715	4.08
Equis monzo-diorite	163-1							156	0.21	653	0.008	13	0.093	1.28	2.68	0.32	13.6
	163-10							95	0.14	244	0.006	9	0.003	0.26	0.83	0.17	4.9
	163-2							123	0.2	526	0.004	10	0.038	0.94	2.09	0.57	11.7
	163-3							169	0.21	894	0.016	12	0.186	2.7	4.25	1.03	21.5
	163-4							114	0.15	375	0.006	11	0.013	0.6	1.44	0.34	7.6
	163-5							118	0.18	499	b.d.l.	15	0.031	0.66	1.56	0.23	9.1
	163-6							120	0.13	341	b.d.l.	10	0.014	0.43	1.14	0.37	7.3
	163-7							206	0.17	487	b.d.l.	8	0.036	0.94	1.77	0.48	10
	163-8							175	0.35	1,617	0.048	17	0.411	5.5	8.52	1.92	36.7
	163-9							150	0.21	545	b.d.l.	12	0.059	1.08	2.17	0.57	12.9
	Av. rock	38.5	0.4	67.45	2.71	1.62	0.53	688	327	18.92	26.9	57.9	6.46	24.4	4.6	0.899	3.78
South grano-diorite	165-1							153	0.13	252	0.246	11	0.022	0.46	0.77	0.3	4.4
	165-10							63	0.26	574	0.006	13	0.12	1.79	3.02	1.14	14.1
	165-2							111	0.25	396	0.009	12	0.034	0.74	1.4	0.28	8.4
	165-4							92	0.18	541	0.002	10	0.078	1	1.79	0.48	10.9

Table 1 (Contd.)

Unit	Analysis[a]	Age (Ma)	±SE	SiO_2	±SD	MgO	±SD	P	Sr	Y	La	Ce	Pr	Nd	Sm	Eu	Gd
	165-5							89	0.14	310	0	9	0.022	0.43	1.21	0.23	5.8
	165-6							129	0.25	630	0.002	20	0.059	1.07	2.1	0.48	12.5
	165-7							102	0.13	296	0.007	11	0.013	0.42	1.51	0.41	5.1
	165-8							64	0.21	267	b.d.l.	11	0.03	0.51	0.76	0.41	4.3
	165-9							113	0.22	507	0.004	16	0.037	1.04	2.49	0.71	11.8
	Av. rock	38	0.3	64.8	3.8	2.16	1.39	811	505	8.87	20.8	40.3	4.33	16.1	2.71	0.768	2.04
El Abra	176-10							60	0.13	186	b.d.l.	10	–0.008	0.16	0.52	0.17	2.7
mine	176-2							61	0.14	287	0.008	10	0.021	0.52	0.89	0.29	4.5
por-	176-3							56	0.19	230	0.001	11	0.023	0.19	0.78	0.24	3.9
phyry	176-4							124	1.88	749	0.021	16	0.039	0.74	1.67	0.49	10.4
	176-5							65	0.19	319	0.004	13	0.003	0.17	0.96	0.25	4.9
	176-6							124	0.34	791	0.018	28	0.068	1.18	1.68	0.66	11.5
	176-7							149	0.17	290	0.142	12	0.031	0.62	0.67	0.19	5.4
	176-8							247	1.11	1,956	1.746	54	0.336	1.74	3.21	0.69	26.1
	176-9							51	0.3	365	0.056	11	0.081	0.63	1.65	0.54	7.1
	Av. rock	37.4	0.3	66.64	3.14	1.41	0.79	637	545	9	19.8	39.6	4.35	16.3	2.7	0.761	2.1
Los Picos-Fortuna suite																	
Los	521-02							338	0.32	1,515	0.006	28	0.204	3.54	6.11	0.48	32.6
Picos	521-03							290	0.23	1,226	0.011	21	0.172	2.68	5.34	0.48	27.1
diorite	521-04							318	0.31	2,033	0.037	19	0.425	5.95	11.9	1.3	60.2
	521-05							351	0.37	1,794	0.009	25	0.156	2.76	5.44	0.51	30.6
	521-06							388	0.39	1,849	0.021	25	0.183	3.31	6.58	0.57	33.9
	521-07							259	0.33	1,498	0.024	15	0.211	3.49	6.43	0.54	35.7
	521-08							230	0.58	1,068	0.106	18	0.136	1.8	3.57	0.31	19.6
	521-09							237	0.42	2,249	0.047	20	0.485	6.88	10.76	0.83	54
	521-10							226	0.46	2,275	0.029	25	0.413	6.68	11.47	0.79	50.3
	Av. rock	42.3	0.2	62.11	3.43	2.5	0.73	784	527	20.34	26.4	56.2	6.56	25.6	4.98	1.014	4.22
Fortuna	98-576.1								0.54		0.014	16	0.069	3.47	3.24	0.41	13.3
Gris	98-576.2								0.49		0.333	9	0.296	2.52	1.02	0.35	7.3
	98-576.3								0.93		0.044	20	0.51	6.45	8.75	1.69	38.8
	98-576.4								0.22		0.019	14	0.37	4.43	5.6	0.77	15.8
	98-576.5								0.76		0.182	13	0.307	2.74	3.14	0.34	10.2
	98-576.6								0.88		0.009	13	0.053	2.63	1.81	0.33	10.4
	98-576.7								0.45		0.703	11	0.221	3.52	2.69	0.66	14.1
	98-576.8								0.17		0.018	9	0.428	4.21	2.35	0.39	12.7
	98-576.9								0.34		0.327	20	0.431	8.06	9.66	1.98	44.2
	98-576.10								0.56		0.004	12	0.219	2.74	2	0.43	6.2
	Av. rock	39.1	0.4	65.28	3.12	1.77	0.62	765	488	16.78	25.9	52.8	6.03	23.1	4.26	0.878	3.41
Fortuna	98-570.1								0.45		0.139	11	0.141	1.7	1.01	0.5	4.5
Clara	98-570.2								0.43		0.152	11	0.46	3.24	3.52	1.29	16.1
	98-570.3								0.51		0.106	15	0.534	2.67	2.92	0.44	9.1
	98-570.4								1.3		0.98	16	0.496	3.32	1.86	0.27	8
	98-570.5								1.55		0.139	11	0.042	2.46	2.33	0.5	8.1
	98-570.6								0.2		0.025	13	0.619	5.64	6.59	1.8	23.6
	98-570.7								0.72		0.011	14	0.142	2.58	1.9	0.61	7.2
	98-570.8								0.31		0.336	20	0.242	3.59	2.32	0.36	8.7
	98-570.9								0.87		0.01	14	0.301	2.94	3.61	0.83	12.2
	98-570.10								0.72		0.156	13	0.501	2.74	1.78	0.24	6
	Av. rock	38.5	0.4	66.49	1.13	1.38	0.2	730	672	9.72	20.6	41.2	4.75	18	3.22	0.811	2.36
Fortuna	98-565.1								0.63		0.033	14	0.517	5.42	6.96	1.38	27.9
leuco-	98-565.2								0.4		0.349	10	0.291	2.07	1.54	0.48	8.1
ganite	98-565.3								1.1		0.365	15	0.301	3.35	3.51	0.61	8.9
	98-565.4								1.83		0.029	12	0.455	2.53	1.35	0.59	8
	98-565.5								1.14		0.004	12	0.174	1.9	2.15	0.77	11.8
	98-565.6								0.99		0.332	15	0.283	2.83	1.62	0.32	9.7
	98-565.7								1.16		0.005	11	0.195	2.38	2.89	0.59	9
	98-565.8								0.51		0.362	12	0.405	4.37	6.72	1.06	26.1
	98-565.9								1.22		0.172	11	0.307	4.18	3.37	0.82	18
	98-565.10								0.49		0.177	13	0.323	5.16	6.22	1.33	26
	Av. rock	38.1	0.4	75.83	3.09	0.17	0.15	95	239	15.27	31.1	66.2	7.51	26.8	4.58	0.572	3.22
San	98-530.1								6.04		8.87	37	2.9	14.17	5.54	0.72	13.9
Lore-	98-530.2								0.9		0.291	16	0.481	3.42	1.34	0.32	7.3
nzo	98-530.3								0.2		0.022	17	0.072	3.47	2.62	0.81	17.2
por-	98-530.4								0.61		0.005	13	0.275	2.61	1.49	0.27	7.4
phyry	98-530.5								0.6		0.004	13	0.273	2.76	1.42	0.28	7.6
	98-530.6								0.59		0.004	26	0.315	3.85	2.56	0.36	13.6
	98-530.7								0.87		0.077	9	0.022	2.32	1.37	0.26	4.9
	98-530.8								1.21		0.143	8	0.153	1.45	0.89	0.54	5.9

Table 1 (Contd.)

Unit	Analysis[a]	Age (Ma)	±SE	SiO_2	±SD	MgO	±SD	P	Sr	Y	La	Ce	Pr	Nd	Sm	Eu	Gd
	98-530.9								0.52		0.009	16	0.32	3.63	2.48	0.67	8.2
	Av. rock	38	0.4	68.27	3.61	0.92	0.43	535	486	8.43	25.6	45.8	4.86	17.3	2.9	0.652	2.02
Chuquicamata Igneous Complex																	
East	610-01							178	0.3	1,436	0.044	19	0.104	1.59	3.29	2.01	23.4
por-	610-02							89	0.29	557	0.062	36	0.05	0.76	1.54	0.75	9.8
phyry	610-03							48	0.12	216	b.d.l.	14	0.015	0.21	0.4	0.24	3.1
	610-04							63	0.29	611	0.014	33	0.046	0.52	1.23	0.54	8.1
	610-05							64	0.39	676	0.496	35	0.098	0.94	1.62	0.68	10
	610-06							106	0.36	813	0.135	50	0.101	1.22	2.67	0.99	15.8
	610-07							69	0.38	968	0.029	42	0.06	1.06	2.53	0.98	14.7
	610-08							46	0.3	859	0.018	40	0.017	0.61	1.7	0.69	11.2
	610-09							99	0.3	735	0.06	21	0.024	0.55	1.41	0.72	9.2
	610-10							101	0.31	1,595	0.016	53	0.139	2.36	5.81	3.29	38.3
	Av. rock	34.6	0.2	67.96	1.6	0.56	0.28	391	354	5.25	20.2	37.6	4	14.4	2.28	0.557	1.43
West	609-01							103	0.27	747	0.03	27	0.065	0.98	2.11	0.84	11.5
por-	609-02							55	0.23	515	0.162	25	0.073	0.55	1.04	0.4	5.6
phyry	609-03							105	0.39	1,635	0.017	73	0.085	1.96	5.03	1.88	32.9
	609-04							88	0.35	1,217		60	0.101	1.32	3.61	1.57	21.6
	609-05							113	0.39	1,441	0.044	63	0.052	1.03	3.28	1.27	23.9
	609-06							74	0.23	823	0.021	37	0.048	0.72	1.67	0.63	11.6
	609-07							97	0.4	1,522	0.019	85	0.08	1.61	3.29	0.86	22.2
	609-08							62	0.32	607	0.076	33	0.063	0.53	1.49	0.57	9.6
	609-09							190	0.34	827	0.027	18	0.041	0.78	2.39	0.54	13.7
	609-10							75	0.72	208	0.156	13	0.115	0.17	0.68	0.2	3.2
	Av. rock	33.5	0.2	71.46	3.14	0.51	0.14	394	364	4.49	17	31.4	3.35	12	1.88	0.501	1.22
Bench	603-01							94	1.25	1,213	0.039	57	0.055	0.97	2.54	1.02	19.1
por-	603-02							83	0.3	751	0.103	30	0.074	0.97	1.9	0.7	12.6
phyry	603-03							79	0.3	539	0.094	22	0.052	0.74	1.2	0.41	6.9
	603-04							93	0.44	1,041	0.077	40	0.239	3.04	4.76	1.3	24.5
	603-05							55	0.23	427	0.073	25	0.038	0.44	0.9	0.39	5.7
	603-06							62	0.26	705	0.013	38	0.038	0.68	1.94	0.8	11.9
	603-07							77	0.31	853	0.038	47	0.045	0.87	2.13	0.81	12.8
	603-08							65	0.52	1,164	0.224	53	0.152	1.85	3.55	1.16	20.6
	603-09							61	0.24	454	0.012	24	0.019	0.43	0.79	0.37	5.6
	603-10							69	0.22	671	0.026	44	0.037	0.92	1.8	0.63	11.2
	Ave rock	33.3	0.3	69.8	1.83	0.45	0.08	349	374	5.02	13.8	25.9	2.78	10.1	1.63	0.454	1.15
Rado-	081-1							60	0.55	927	0.105	44	0.085	0.88	1.87	0.71	12.4
miro	081-10							65	0.32	898	0.005	37	0.038	0.65	1.69	0.66	11
Tomic	081-2							50	0.26	580	0.011	21	0.09	1.06	2.31	0.83	10.6
minor	081-3							75	0.32	724	0.14	34	0.069	0.71	1.52	0.63	9.9
facies	081-4							87	0.36	1,236	0.004	48	0.049	1.15	2.56	1.24	19.5
por-	081-5							91	0.34	920	0.02	43	0.043	1.01	1.96	0.79	13.7
phyry	081-6							54	0.22	615	0.002	38	0.027	0.71	1.6	0.69	9.4
	081-7							56	0.29	806	0.007	36	0.003	0.62	1.47	0.63	10.3
	081-8							50	0.27	636	0.062	30	0.057	0.58	1.2	0.41	8.2
	081-9							93	0.36	1,090	0.054	51	0.065	1.23	3.2	1.12	19
	Av. rock	34	0.4	70.77	1.38	0.36	0.07	326	600	4.62	15.8	30.3	3.19	11.8	1.91	0.576	1.29
Rado-	695-1							75	0.3	668	0.004	21	0.044	0.91	1.98	0.72	10.9
miro	695-10							54	0.29	566	0.001	24	0.031	0.42	1	0.42	7.1
Tomic	695-2							56	0.35	841	0.002	34	0.015	0.56	1.44	0.82	10.9
major	695-3							81	0.37	619	0.019	40	0.059	0.82	2.11	0.78	11.4
facies	695-4							62	0.31	790	0.003	39	0.07	1.04	3.15	1.24	16.4
por-	695-5							86	0.27	447	0.009	17	0.013	0.26	0.81	0.31	5.1
phyry	695-6							55	0.33	744	0.005	33	0.009	0.58	1.24	0.6	8.4
	695-7							50	0.25	430	0.006	24	0.023	0.48	0.88	0.43	6
	695-8							67	0.32	732	0	32	0.032	0.46	1.69	0.57	10.3
	695-9							105	0.55	1,797	0.019	68	0.087	1.77	4.42	1.52	27.5
	Av. rock	34.6	0.4	70.86	1.4	0.45	0.24	348	416	4.08	15.3	28.9	2.96	10.6	1.63	0.465	1.12
Others																	
Monte-	626-1							147	0.25	1,111	0.073	12	0.531	6.99	9.26	1.24	35.1
cristo	626-10							190	0.24	756	0.011	9	0.098	1.55	3.27	0.5	18.3
Intru-	626-2							163	0.21	700	0.01	8	0.109	1.82	3.35	0.52	17.4
sive	626-3							158	0.27	1,138	0.061	13	0.514	7.09	9.65	1.07	37.3
	626-4							163	0.18	779	0.02	9	0.24	3.48	5.06	0.73	22.7
	626-5							139	0.15	448	0.007	8	0.051	0.83	1.75	0.27	9.7
	626-6							172	0.2	725	0.013	9	0.137	2	3.76	0.52	18.8
	626-7							145	0.2	693	0.015	9	0.172	2.82	4.31	0.53	19.2
	626-8							129	0.16	394	0.002	8	0.039	0.7	1.56	0.23	8.2

Table 1 (Contd.)

Unit	Analysis[a]	Age (Ma)	±SE	SiO_2	±SD	MgO	±SD	P	Sr	Y	La	Ce	Pr	Nd	Sm	Eu	Gd
	626-9							177	0.22	564	0.056	8	0.075	0.99	2.04	0.34	12.4
	Av. rock	63.2	0.5	63.52	3.49	2.23	0.62	1,039	362	27.8	31.4	67.3	7.8	30.2	5.97	1.02	5.33
Opache	067-1							58	0.28	483	0.001	18	0.015	0.38	0.96	0.31	5.8
mine	067-10							116	0.26	995	0.001	15	0.093	2.27	5.17	1.15	26
por-	067-2							61	0.13	275	0.004	15	b.d.l.	0.23	0.85	0.19	4.3
phyry	067-3							99	0.32	757	0.014	29	0.054	1.33	2.29	0.97	13.3
	067-4							91	0.17	296	0.024	7	0.053	0.63	1.16	0.14	5.6
	067-5							84	0.17	312	0.009	14	0.008	0.47	1	0.32	5.3
	067-6							100	0.19	333	0.005	13	0.025	0.67	1.45	0.39	7.2
	067-7							67	0.17	290	b.d.l.	12	0.017	0.2	0.75	0.32	4.5
	067-8							123	0.27	745	0.005	13	0.114	1.87	3.66	0.93	16.8
	067-9							70	0.22	326	0.006	13	0.028	0.48	0.99	0.39	5.7
	698-1							84	0.15	252	0.005	11	0.014	0.43	0.97	0.3	4.6
	698-10							114	0.22	609	0.006	22	0.073	1.33	2.58	0.66	12.4
	698-2							93	0.18	446	0.007	12	0.014	0.6	1.35	0.46	8.4
	698-3							99	0.19	407	0.009	12	0.039	0.5	1.49	0.33	7.8
	698-4							79	0.17	274	b.d.l.	11	0.027	0.38	0.87	0.32	5
	698-5							81	0.23	562	0.009	28	0.05	0.95	1.73	0.49	8.9
	698-6							82	0.18	374	0.002	10	0.068	1.33	2.06	0.68	9
	698-7							54	0.16	259	0.005	9	0.041	0.51	0.66	0.3	4.6
	698-8							64	0.25	558	0.004	12	0.104	1.92	3.5	1.16	14.1
	698-9							75	0.16	252	0.004	12	0.023	0.34	0.96	0.37	4.6
	Av. rock	37.9	0.2						543	7.33	21	41.6	4.51	17.1	2.81	0.809	1.99
Elena	679-1							77	0.27	487	0.029	18	0.037	0.64	1.21	0.66	8.5
grano-	679-4							49	0.41	233	0.137	11	0.054	0.43	0.39	0.21	2.9
diorite	679-5							81	0.33	746	0.006	33	0.041	1.05	2.33	0.81	13.3
	679-6							52	0.14	172	0.007	9	0.013	0.12	0.5	0.14	2.9
	679-7							81	0.22	461	0.098	12	0.097	1.15	2.23	0.64	9.9
	679-8							58	0.28	513	0	25	0.027	0.42	1.23	0.46	7.1
	679-9							80	0.21	328	0.029	13	0.022	0.44	0.88	0.34	5.3
	Av. rock	37.7	1						532	6.37	19.9	36.1	3.7	13.3	2.15	0.561	1.5

[a]SiO_2 and MgO are given in wt%, all other concentrations are reported in ppm. SE, Standard error; SD, standard deviation; b.d.l., below detection limit

increasingly incompatible in plagioclase at higher oxidation states, reflecting a larger proportion of Eu(III) in the magma (Drake 1975; Wilke and Behrens 1999). Thus, if plagioclase fractionation is accompanied by progressive oxidation, the expected trend of decreasing Eu_N/Eu_N^* during differentiation can be retarded, which is what is observed in the the Los Picos-Fortuna/Pajonal-El Abra complex (Ballard et al., unpublished data).

Although both the Ce(IV)/Ce(III) and Eu_N/Eu_N^* ratios in zircon can be used as a measure of magmatic oxidation state, we prefer Ce(IV)/Ce(III) over Eu_N/Eu_N^* for two reasons. First, the Ce(IV)/Ce(III) ratio is more sensitive, varying by almost two orders of magnitude in the zircons of this study compared to a factor of five range in Eu_N/Eu_N^* (Fig. 8). Second, the interpretation of Eu_N/Eu_N^* in zircon is complicated by the competing influences of plagioclase crystallization and assimilation of plagioclase-bearing rocks, which can change the Eu_N/Eu_N^* of the melt.

Mechanism of magma oxidation

The zircon REE data suggest that the Los Picos-Fortuna/Pajonal-El Abra igneous complex became progressively more oxidized over time. Previous workers have attributed positive shifts in magmatic oxidation state to (1) metasomatism of a mantle source region prior to or during partial melting, induced by hydrous fluids or silicate melts derived from subducted oceanic crust and enriched in oxidized components such as Fe(III), CO_2 or sulfate (McInnes and Cameron 1994); (2) fractional crystallization of Fe(II)-bearing silicate, oxide or sulfide phases in a closed-system magma chamber (Carmichael and Ghiorso 1986); (3) influx of SO_2 into an evolved felsic magma chamber from degassing mafic magma ponded below it (Matthews et al. 1992; Pallister et al. 1992); and (4) degassing of hydrous magma at low pressures with preferential removal of reduced volatile species such as H_2 or H_2S (Czamanski and Wones 1973; Candela 1986; Ague and Brimhall 1988). Assimilation of oxidized country rock could be added to this list. As noted above, we interpret the Los Picos-Fortuna/Pajonal-El Abra igneous complex to have been sourced from an episodically replenished, long-lived magma reservoir at depth. If this interpretation is correct, then the systematic increase in zircon Ce(IV)/Ce(III) ratios with time (Fig. 10) means that progressive oxidation within the parental magma reservoir was not interrupted or reversed by injection of new magma or extraction of resident magma. This argues that oxidation did not occur in association with high-level emplacement of individual intrusions, but by processes within or below the hypothesized deep magma reservoir.

Table 2 Zircon and whole-rock trace-element data: Tb, Dy, Ho, Er, Tm, Yb, Lu, Th, U, Zr, Hf, Eu/Eu*, and Ce(IV)/Ce(III)

Unit	Analysis[a]	Tb	Dy	Ho	Er	Tm	Yb	Lu	Th	U	Zr	Hf	Eu/Eu*	±SD	Ce(IV)/Ce(III)	±SD
Pajonal-El Abra suite																
Pajonal diorite	195-1	14.52	153.4	53.7	228.6	46	408	70.1	494	453		8,515	0.13		11	
	195-10	15.94	164.7	57.2	247	50.1	445	76.5	493	445		8,836	0.13		11	
	195-2	14.91	153.4	52.1	222.6	46.2	412	69.7	533	544		10,070	0.09		14	
	195-4	15.04	153.9	51.9	222	45.8	412	69.1	498	506		9,855	0.11		12	
	195-5	8.52	92	32.7	142.6	30.9	286	49.5	271	312		10,232	0.11		46	
	195-6	15.04	156.4	53.4	228.1	47.4	425	71.3	531	555		10,012	0.09		13	
	195-7	14.59	173.9	66.1	314.2	72	684	116.9	1,331	3,636		14,007	0.05		152	
	195-8	15.53	165.9	58.9	258.2	52	464	78.7	668	684		8,968	0.09		11	
	195-9	13.9	142.7	48.4	208.7	43.3	389	65.4	436	434		9,573	0.11		14	
	Av. zircon												0.1	0.02	32	46
	Av. rock		4.316	0.848	2.394		2.492	0.358	32.11	8.66	283.7	7.5				
Apolo leuco-granite	174-1	9.39	99.4	33.7	151.2	32.5	284	49.6	171	164		7,685	0.24		8	
	174-10	3.48	42.2	14.7	69.4	15.6	156	27.3	71	88		8,064	0.26		49	
	174-2	7.6	79.6	25.7	110.7	23.5	213	35.3	138	135		8,682	0.19		6	
	174-3	5.03	56.7	20	89.2	20	189	32.3	119	143		8,445	0.24		37	
	174-4	2.9	33.9	12.2	58.9	13.3	131	23.2	64	93		7,778	0.22		47	
	174-5	3.16	35.8	13.1	61.9	14.3	136	24.3	85	118		8,389	0.21		57	
	174-6	2.42	28.9	10.2	48.6	11.8	128	27.5	69	614		9,604	0.24		70	
	174-7	3.07	33.5	12.1	57.2	12.8	128	22.6	80	106		8,323	0.18		107	
	174-8	3.21	39.9	13.8	63.2	14.5	141	24.9	83	104		8,456	0.23		46	
	174-9	3.24	37	13.2	63.8	14.6	145	25.6	78	108		8,585	0.18		88	
	Av. zircon												0.22	0.03	52	32
	Av. rock		2.183	0.434	1.271		1.55	0.232	26.16	8.62	191.2	5.74				
Central diorite	131-1	7.47	82.2	29.2	133.2	29.6	279	50.1	209	214		8,284	0.23		54	
	131-10	4.77	56.4	20	93	20.6	199	35.1	109	123		9,473	0.25		100	
	131-3	17	194.7	68.5	310.5	64.7	589	103.1	506	380		8,291	0.23		22	
	131-4	6.58	77.4	28.1	137.4	31.8	315	58.8	197	234		9,640	0.27		88	
	131-6	7.6	80.2	27.4	124	27	247	43	138	134		9,414	0.25		28	
	131-7	4.86	54.6	18.4	85.7	19.2	186	33.1	91	95		8,906	0.23		37	
	131-8	14.31	161.2	55.8	252.8	54.2	509	88	445	361		8,517	0.21		28	
	131-9	5.86	67.1	23.8	113.8	25.4	244	42.8	128	159		10,226	0.27		61	
	Av. zircon												0.24	0.02	52	29
	Av. rock		3.437	0.655	1.878		1.914	0.277	19.4	5.37	198.8	5.18				
Dark diorite	180-1	11.64	131.4	48.6	228	50.7	495	89.5	1,432	1,199		9,731	0.28		202	
	180-10	14.37	164.1	62.6	300.4	72.2	740	130	947	1,575		13,086	0.25		161	
	180-2	32.11	330.1	114.7	506.1	107.7	987	176.7	836	653		8,134	0.38		25	
	180-3	11.35	128.4	47	221.7	48.8	489	91.8	400	933		11,325	0.37		89	
	180-4	37.8	394	136.4	593.4	124.1	1,173	205.7	1,015	629		8,335	0.4		27	
	180-5	15.43	168.4	60.2	273.1	60.5	575	106.5	367	479		9,062	0.4		37	
	180-6	12.87	148.8	55.2	253.4	56.1	565	103.3	494	636		9,986	0.32		74	
	180-7	26.23	279	99.6	432.2	93.2	882	156.9	730	442		7,886	0.4		35	
	180-8	20.48	219.8	77.9	347.5	74.9	716	123.9	562	466		9,754	0.35		31	
	180-9	17.02	182.5	63.8	278	60	576	101.1	359	286		8,569	0.42		27	
	Av. zircon												0.36	0.06	71	63
	Av. rock		2.774	0.528	1.496		1.525	0.218	5.52	1.96	96.6	2.54				
Aplite	121-1	5.24	54.7	19.3	87.5	19.3	185	34.4	63	79		8,799	0.34		38	
	121-10	2.62	29.1	11.3	52.7	12.4	122	23.4	57	82		9,102	0.26		138	
	121-2	3.56	41.1	15.1	69.4	16	158	28.6	91	120		9,557	0.24		111	
	121-3	4.78	54.9	19.3	89.2	20.1	192	34.7	99	113		9,286	0.27		77	
	121-4	3.49	39	13.6	64.3	14.5	143	26.7	75	95		9,194	0.29		118	
	121-5	3.89	45.4	18.1	89	20.9	214	41.1	115	178		10,384	0.3		284	
	121-6	10.17	110.5	39.1	174	38.3	356	63.9	211	200		8,586	0.32		20	
	121-7	2.45	29	10.7	50.9	11.6	117	22.1	45	64		9,471	0.27		121	
	121-8	5.02	55.3	19	86.6	19.3	185	33.6	101	111		9,492	0.25		45	
	121-9	4.51	49.4	17.6	84.7	19.4	190	36.4	115	157		9,779	0.28		115	
	Av. zircon												0.28	0.03	107	74
	Av. rock		3.749	0.725	2.071		2.287	0.344	55.49	17.55	201.9	6.16				
Equis mon-zodio-rite	163-1	4.99	59.5	20.6	94.7	21.6	204	36.3	166	346		1,0619	0.16		67	
	163-10	1.7	21.1	7.6	37.2	8.9	91	17.1	35	61		9,544	0.26		224	
	163-2	4.27	49.2	16.9	77.9	17.4	170	32.1	64	78		8,458	0.35		76	
	163-3	7.18	82.7	29.3	135.3	30.2	286	53.3	123	134		9,057	0.33		35	
	163-4	2.88	32.7	11.7	55.8	12.9	130	23.9	59	84		9,169	0.31		130	
	163-5	3.62	43	15.8	77.4	18.1	178	32	120	170		10,554	0.18		200	
	163-6	2.63	30.2	10.7	50.9	11.8	118	21.9	55	81		8,757	0.39		173	
	163-7	3.69	42.9	15.6	74.8	17.3	172	33.2	43	68		8,242	0.35		89	
	163-8	12.58	145.6	53	243.3	52.6	492	91.2	277	256		8,243	0.33		21	

Table 2 (Contd.)

Unit	Analysis[a]	Tb	Dy	Ho	Er	Tm	Yb	Lu	Th	U	Zr	Hf	Eu/Eu*	±SD	Ce(IV)/Ce(III)	±SD
	163-9	4.2	49.4	17.6	84.2	19.7	194	35.8	74	103		9,906	0.33		94	
	Av. zircon												0.3	0.08	111	69
	Av. rock		3.383	0.66	1.903		1.996	0.294	28.04	8.45	194.5	5.41				
South	165-1	1.61	20.4	7.4	38.7	10.1	108	23.9	92	131		8,009	0.49		440	
grano-	165-10	4.89	49.2	18	84.8	20.6	215	42.7	146	167		9,044	0.53		61	
diorite	165-2	3.03	34.6	12.8	58.5	13.9	133	24.7	71	96		8,256	0.25		151	
	165-4	3.86	47.7	17.6	84.3	19.6	185	36.5	96	106		8,471	0.33		111	
	165-5	2.23	25.8	9.6	46.3	11.2	114	21.6	39	65		8,562	0.26		138	
	165-6	4.76	54.3	19.8	94.3	21.7	202	38.6	223	213		8,671	0.29		174	
	165-7	2.07	25.1	9.2	43	10.7	111	22.5	65	91		7,573	0.45		112	
	165-8	1.78	21.2	7.7	41.8	11	122	25.2	84	147		9,820	0.68		468	
	165-9	4.06	43.6	16.4	77.2	18.4	182	34.9	57	84		8,310	0.4		93	
	Av. zircon												0.41	0.14	194	151
	Av. rock		1.676	0.308	0.889		0.979	0.151	7.69	2.61	94.4	2.66				
El Abra	176-10	1.16	13.9	5.5	29.2	8	87	19.1	57	121		9,254	0.44		797	
mine	176-2	1.8	21.3	8.5	44.4	11.3	126	26.6	101	137		7,912	0.44		379	
por-	176-3	1.49	18	6.9	35.6	9.4	107	22	55	106		8,989	0.43		428	
phyry	176-4	4.28	54	22.9	121.2	30.6	338	69	99	146		8,478	0.36		414	
	176-5	1.9	23.9	9.5	50.4	13.2	157	34.3	144	248		9,674	0.36		515	
	176-6	4.97	59.4	24	122.2	30.5	319	64.2	268	333		7,649	0.46		677	
	176-7	2.03	25.2	9.3	44.7	10.1	107	21	60	105		8,169	0.31		606	
	176-8	11.05	148.7	61.2	311.7	78	821	160	445	1,075		12,826	0.23		868	
	176-9	2.32	29.6	10.8	54.3	13.9	155	30.7	78	120		10,425	0.48		142	
	Av. zircon												0.39	0.08	536	226
	Av. rock		1.661	0.309	0.882		0.957	0.137	7.83	2.59	112	3.05				
Los Picos-Fortuna suite																
Los	521-02	11.6	130.3	47.2	215.5	43.9	386	72.9	540	541		8,821	0.1		63	
Picos	521-03	9.53	107.2	38.9	175	35.6	308	57.3	339	365		7,949	0.12		50	
diorite	521-04	19.45	206.7	69.1	286.8	55.2	454	79.1	485	393		7,128	0.15		11	
	521-05	11.48	139.4	55.3	269.7	57.7	525	102.8	399	603		8,020	0.12		102	
	521-06	12.81	150.4	57.7	276.5	57.8	517	97.4	588	627		7,327	0.12		65	
	521-07	12.37	137.3	49	212.6	42.4	374	68.9	282	324		7,948	0.11		29	
	521-08	7.5	87.5	33.3	156	33	308	59.7	227	358		9,786	0.11		100	
	521-09	18.89	208.6	72.4	314.1	61.5	525	93.7	456	433		8,943	0.11		18	
	521-10	17.93	202	73.2	327.4	64.8	561	102.4	584	604		10,067	0.1		22	
	Av. zircon												0.12	0.01	51	34
	Av. rock	0.602	3.808	0.742	2.105		2.174	0.32	21.88	5.46	231.3	6.33				
Fortuna	98-576.1	4.8	66.3	23.6	106.3	24.2	281	45.2	126	167		2,683	0.19		97	
Gris	98-576.2	2.45	27.2	9	45.4	10.9	147	19.3	39	68		2,332	0.39		215	
	98-576.3	11.55	147.6	50.2	216	47.3	459	79.7	323	279		2,338	0.28		27	
	98-576.4	5.23	66.2	22.3	102.4	23.3	254	41.7	128	153		2,319	0.25		26	
	98-576.5	3.23	43.1	15.3	68.5	16	192	28.7	89	114		2,220	0.18		53	
	98-576.6	3.29	44.1	14.7	73	16.2	197	30	88	126		2,231	0.23		158	
	98-576.7	4.36	56.7	18.6	90.1	20.1	227	35.3	84	114		2,054	0.32		73	
	98-576.8	2.9	43.8	14.8	70	16.1	185	28	57	81		2,044	0.22		63	
	98-576.9	13.52	156.6	55.5	243	51.4	511	86.5	306	263		2,081	0.29		24	
	98-576.10	1.98	28.7	11.1	54.4	12.3	169	24.7	59	110		2,214	0.37		106	
	Av. zircon												0.27	0.07	84	62
	Av. rock	0.481	2.967	0.565	1.589		1.674	0.247	15.98	3.89	178.1	4.58				
Fortuna	98-570.1	1.7	24.5	8.4	40.9	10.4	149	22.9	59	98		1,862	0.72		315	
Clara	98-570.2	4.89	62.5	22.7	106.1	23.5	275	46.8	83	108		1,708	0.52		53	
	98-570.3	3.46	46	15.3	74.7	16.5	201	31.9	84	118		1,645	0.26		73	
	98-570.4	2.82	35.6	12.7	55.7	13.9	176	26.8	54	76		1,516	0.21		212	
	98-570.5	2.76	36.8	12.6	56.4	14.3	185	28.6	43	194		1,533	0.35		75	
	98-570.6	7.71	96	31.1	133.7	29.5	311	51.9	87	101		1,236	0.44		20	
	98-570.7	2.97	38	14.7	73.5	17.8	225	35	89	145		2,484	0.5		187	
	98-570.8	3.58	45.6	17	78.3	20.2	241	38.5	163	250		2,439	0.24		185	
	98-570.9	4.33	52.6	17.1	79	18.7	219	32.8	89	104		2,130	0.38		50	
	98-570.10	2.5	31.6	10.3	51.2	12.5	166	23.7	59	102		2,151	0.22		115	
	Av. zircon												0.38	0.16	129	93
	Av. rock	0.313	1.86	0.349	0.973		1.053	0.159	9.44	3.02	99	3.56				
Fortuna	98-565.1	8.06	99.5	34	146.3	31.9	321	56.4	150	158		2,001	0.3		8	
leuco-	98-565.2	2.5	35.3	13.2	58.4	14	166	27.3	46	74		2,149	0.41		62	
granite	98-565.3	2.61	36.9	13.6	63.3	15.6	182	28.3	91	135		2,263	0.33		18	
	98-565.4	2.83	30.9	11.9	52.8	12.4	154	23.1	66	93		2,121	0.54		81	
	98-565.5	3.19	38.4	14.2	66.6	15.5	184	30.2	81	118		2,169	0.47		41	
	98-565.6	3	41.7	15.6	68.5	16.1	198	29.9	112	154		2,334	0.25		85	

Table 2 (Contd.)

Unit	Analysis[a]	Tb	Dy	Ho	Er	Tm	Yb	Lu	Th	U	Zr	Hf	Eu/Eu*	±SD	Ce(IV)/Ce(III)	±SD
	98-565.7	2.84	35.9	14.2	62.1	15	182	27.4	86	113		2,216	0.35		18	
	98-565.8	7.99	90.5	31.9	130.3	27	264	42.2	188	175		2,124	0.24		5	
	98-565.9	5.55	60.6	22.5	100.4	22.8	243	38.8	87	99		2,166	0.32		19	
	98-565.10	7.64	84.9	30.7	131.2	29.1	285	45.4	115	121		2,062	0.32		8	
	Av. zircon												0.36	0.1	37	31
	Av. rock	0.443	2.706	0.532	1.577		1.93	0.297	29.5	7.06	87	3.18				
San	98-530.1	4.37	60.8	23.1	106.6	26.9	315	57.2	112	196		2,080	0.25		122	
Lore-	98-530.2	2.44	40.1	14.7	70	17.5	237	35.8	150	243		2,395	0.31		302	
nzo	98-530.3	5.57	66.7	23.4	104.5	24	284	44.3	121	144		2,300	0.37		103	
por-	98-530.4	3.19	41.2	16.5	81.4	20.8	264	43	99	138		2,323	0.25		282	
phyry	98-530.5	3.14	41.5	16.3	81.2	20.4	261	42.8	101	145		2,373	0.26		279	
	98-530.6	4.48	54.2	21	103.3	26.2	323	53.3	248	478		2,870	0.19		220	
	98-530.7	1.46	24.5	9.1	43.1	10.8	153	22.9	66	165		2,271	0.3		112	
	98-530.8	1.79	21.7	8	37.4	9.1	129	17.7	32	56		2,147	0.72		191	
	98-530.9	2.69	33.1	12.6	64.5	15.6	206	32	102	193		2,549	0.45		90	
	Av. zircon												0.34	0.16	189	85
	Av. rock	0.263	1.568	0.293	0.84		0.983	0.148	15.19	4.09	117.9	3.46				
East	610-01	9.21	112.4	43.9	210.8	45.4	449	92.7	35	80		6,674	0.46		172	
por-	610-02	3.44	39.9	15.2	78.6	19	212	49.2	513	663		10,153	0.53		817	
phyry	610-03	1.16	14.6	6	32.8	8.5	99	24.3	84	202		11,411	0.53		2,214	
	610-04	3.12	39	16.3	88.4	22.5	258	62.5	294	509		10,060	0.77		1,497	
	610-05	3.66	44.6	18.3	97.7	24.6	278	66.3	274	417		9,730	0.63		973	
	610-06	5.55	64.8	23.9	114.8	26.9	274	59	607	580		9,729	0.4		443	
	610-07	5.42	64.9	26.7	137	33.8	371	86.4	276	418		10,360	0.36		629	
	610-08	4.45	56.8	23.6	123.6	31.4	353	83.7	247	412		10,640	0.7		1,259	
	610-09	3.7	46.9	19.9	106	26.9	307	72.5	122	308		10,160	0.5		836	
	610-10	12.88	139.7	50.2	222.5	48.4	467	93.7	233	303		8,390	0.42		154	
	Av. zircon												0.53	0.13	899	632
	Av. rock	0.172	0.949	0.168	0.476		0.558	0.089	7.39	2.38	98.7	2.84				
West	609-01	4.23	49.5	19.7	103.4	26.4	296	69.4	217	399		9,974	0.46		356	
por-																
phyry																
	609-02	2.21	29.2	12.8	74.3	20.3	248	62.1	189	410		11,684	0.74		1,222	
	609-03	11.33	127	47.2	229.4	51.9	530	112	524	614		10,260	0.48		265	
	609-04	7.89	93.1	35	174.3	39.8	409	90.7	507	642		9,561	0.57		346	
	609-05	9.08	107.7	42.2	208.2	48.2	492	104.7	333	567		10,161	0.56		498	
	609-06	4.21	52.5	21.7	117.3	28.3	311	70.8	144	332		9,816	0.44		785	
	609-07	8.39	99.8	40.5	211.1	52.2	550	127	789	838		9,324	0.56		832	
	609-08	3.48	41.2	16.7	87	21.6	233	54.3	242	426		10,690	0.38		679	
	609-09	5.07	62.2	25.5	124.1	29.6	293	65.3	105	155		7,750	0.29		171	
	609-10	1.15	13.9	5.9	32.2	8.4	93	23.2	89	177		9,640	0.95		554	
	Av. zircon												0.54	0.19	571	317
	Av. rock	0.146	0.806	0.149	0.429		0.508	0.081	5.08	2.85	91	2.61				
Bench	603-01	7.36	87.5	35.1	172.3	41.1	428	92.1	350	609		11,062	0.44		879	
por-	603-02	4.95	58.3	22.6	111.9	26.3	267	56.5	278	378		10,851	0.44		506	
phyry	603-03	2.54	33	14.1	78	20.7	252	62.7	164	399		10,951	0.44		1,109	
	603-04	7.53	79.4	28.6	136.6	31.8	350	77.5	340	482		10,772	0.37		157	
	603-05	2.11	26.3	11.2	61.2	16	185	43.5	154	354		10,505	0.52		1,535	
	603-06	4.2	48.6	19.4	99.7	24.7	277	65.1	373	534		10,704	0.51		739	
	603-07	4.58	55.7	22.8	120.1	30.4	345	81	512	764		10,529	0.47		944	
	603-08	7.26	84.4	33.7	169.7	41.9	463	104.9	648	755		12,286	0.41		502	
	603-09	2.09	26.9	11.7	67.2	17.6	210	53.4	184	405		9,643	0.54		2,341	
	603-10	3.89	46	18.3	94.9	23	256	56.3	300	453		10,752	0.43		854	
	Av. zircon												0.46	0.05	957	613
	Av. rock	0.143	0.848	0.156	0.438		0.492	0.074	3.73	2.26	92.7	2.56				
Rado-	081-1	4.83	61.3	26.4	137.2	35.5	405	89.3	347	585		10,055	0.45		1,323	
miro	081-10	4.4	58.2	24.1	132.7	35.5	412	91.7	246	518		10,786	0.47		1,405	
Tomic	081-2	3.56	41.8	16.6	84.3	22	251	54.9	165	305		10,811	0.51		271	
minor	081-3	3.81	47.2	20.2	109.6	29.4	338	77.5	258	494		11,021	0.49		1,388	
facies	081-4	7.61	93.7	37.2	179.6	46.6	480	96.8	234	454		11,202	0.54		823	
por-	081-5	5.36	66.2	26.6	136	34.9	385	83.3	343	566		10,192	0.47		1,096	
phyry	081-6	3.58	42	17.2	86.4	22.4	254	52.2	334	525		12,461	0.54		930	
	081-7	4	52.5	22.2	121	32.3	371	84.3	218	456		10,511	0.5		1,661	
	081-8	3.09	41.1	17.8	95.6	26.4	301	70.1	196	385		10,268	0.4		1,737	
	081-9	6.77	81	31.1	154.7	39.1	421	86.5	421	575		10,338	0.44		516	
	Av. zircon												0.48	0.04	1,115	481
	Av. rock		0.886	0.16	0.468		0.519	0.082	3.63	1.62	99	2.71				

Table 2 (Contd.)

Unit	Analysis[a]	Tb	Dy	Ho	Er	Tm	Yb	Lu	Th	U	Zr	Hf	Eu/Eu*	±SD	Ce(IV)/Ce(III)	±SD
Rado-	695-1	4.11	48.4	18.7	95.8	25.3	285	59.2	130	268		12,587	0.47		313	
miro	695-10	2.69	34.7	15.3	83.6	23.4	282	65.4	119	268		11,693	0.49		1,571	
Tomic	695-2	4.54	55.5	24.1	131.5	36.3	445	103.8	276	595		12,857	0.63		1,684	
major	695-3	4	47	18.2	90	22.7	248	53	438	487		10,365	0.48		485	
facies	695-4	5.33	64.1	23.8	119.1	29.4	325	66.5	342	392		11,790	0.53		262	
por-	695-5	2.05	27.3	12.3	65.2	17.9	216	49	90	228		9,998	0.46		1,249	
phyry	695-6	3.44	43.7	19.7	110.6	30.9	387	85.7	213	452		12,702	0.57		1,820	
	695-7	2.38	28.9	12.1	64.5	17.2	210	47.5	171	338		12,525	0.57		1,457	
	695-8	4.01	50.8	21.1	107.9	28.8	334	70.6	158	298		11,680	0.42		795	
	695-9	10.52	126.2	51	259.8	67.8	772	162.7	2,628	2,194		12,072	0.42		560	
	Av. zircon												0.5	0.07	1,020	601
	Av. rock		0.767	0.137	0.401		0.484	0.076	5.23	2.86	89.1	2.49				
Others																
Monte-	626-1	11.33	114	37.5	154.2	32.1	277	47.1	147	137		8,613	0.21		6	
cristo	626-10	6.47	71.3	24.4	108.1	22.8	210	35.5	92	103		9,348	0.2		31	
Intru-	626-2	6.04	67.1	22.6	100.5	21.6	196	34	87	100		8,562	0.21		25	
sive	626-3	11.66	117.9	38.3	157.3	32.4	280	47.2	150	134		8,701	0.17		6	
	626-4	7.21	76.2	25.6	108.6	23.4	207	35.7	93	102		8,992	0.21		12	
	626-5	3.54	40.9	14.6	65.3	14.9	137	24.8	66	92		8,803	0.2		64	
	626-6	6.29	69.5	23.4	102.9	21.9	199	34.7	90	100		8,854	0.19		23	
	626-7	6.2	69.2	22.9	99.7	21.2	191	33	86	97		8,890	0.18		15	
	626-8	2.96	34.2	12.5	58.2	12.9	123	21.9	55	82		9,032	0.19		71	
	626-9	4.5	51.7	17.9	81.5	17.9	166	28.8	73	90		8,773	0.21		56	
	Av. zircon												0.2	0.01	31	24
	Av. rock	0.8	5.05	1.01	2.86		3.01	0.44	24	6.98	284	8.49				
Opache	067-1	2.41	31.2	13	76.2	22.1	266	60.9	315	677		11,562	0.4		391	
mine	067-10	9.11	95.6	33.2	143.2	31.6	292	51.2	108	119		9,687	0.3		201	
por-	067-2	1.83	20.4	7.9	42	11.6	126	25.1	67	134		12,763	0.3		342	
phyry	067-3	5.1	64.2	25.4	133.7	33.2	386	75.4	222	321		12,647	0.54		222	
	067-4	2.06	24.2	9.1	43.5	10.4	107	21.9	84	436		11,317	0.17		551	
	067-5	1.99	23.9	9.4	48.8	12.5	140	29.7	128	207		10,673	0.42		728	
	067-6	2.73	30	10.7	51.3	12.2	120	23.6	44	61		8,236	0.36		109	
	067-7	1.85	21.6	8.5	45.1	11.8	132	27.5	72	131		10,251	0.53		752	
	067-8	6.21	67.5	24.5	113.9	26.5	264	48.6	93	112		9,966	0.36		57	
	067-9	2.07	23.8	9.7	50.9	13.8	162	35.3	169	406		10,454	0.49		411	
	698-1	1.69	19.5	7.6	38.1	10	114	24	73	112		9,591	0.43		1,698	
	698-10	4.37	50.1	18.9	90	21.9	219	42	159	184		9,943	0.36		40	
	698-2	3.1	36.9	13.9	67.7	17	179	35.9	105	150		10,206	0.42		713	
	698-3	2.91	33.3	12.5	59.9	14.8	151	29.8	69	111		9,544	0.29		591	
	698-4	1.82	21.2	8.4	42	11.2	125	26.2	68	116		10,077	0.46		155	
	698-5	3.47	42.2	16.9	85.2	23.7	261	55	469	501		10,480	0.38		593	
	698-6	2.81	32	11.7	56.9	14.2	149	31.5	75	104		9,115	0.48		203	
	698-7	1.61	20.7	8	40.5	11.2	121	24.9	50	95		11,295	0.52		858	
	698-8	4.24	48.2	16.5	78	19.5	200	39.7	106	135		10,626	0.5		68	
	698-9	1.69	20.7	7.9	38.8	9.9	109	22.8	106	132		9,539	0.54		695	
	Av. zircon												0.41	0.1	469	393
	Av. rock		1.416	0.257	0.715		0.751	0.112	6	2.09	98.6	2.74				
Elena	679-1	3.07	37.2	15	79.4	20.1	224	48.4	101	195		1,1835	0.63		548	
grano-	679-4	1.12	12.9	5.6	31.6	9.2	118	31.3	72	183		9,777	0.61		2,205	
diorite	679-5	5.09	61.1	23.4	118.4	29.5	310	61.7	165	241		11,433	0.44		349	
	679-6	1.07	13.4	5.2	28.7	7.4	87	18.2	51	111		11,791	0.35		642	
	679-7	3.37	38.8	14.1	70.8	17.7	194	38.6	96	129		10,116	0.42		91	
	679-8	2.88	36.9	15.1	81.5	21.1	247	56.4	122	229		11,663	0.47		867	
	679-9	2.13	25.1	10	51.8	13.1	147	29.7	73	131		10,713	0.49		488	
	Av. zircon												0.49	0.1	741	689
	Av. rock		1.171	0.22	0.638		0.724	0.112	5.1	1.49	107.6	3.03				

[a]All concentrations are reported in ppm. SD, Standard deviation

Sulfur speciation and its control on chalcophile element behavior in magmas

Although there is a well-known empirical association between Cu ± Au mineralization and oxidized calc-alkaline intrusions, the cause of this relationship is uncertain. Oxidation state controls sulfur speciation and hence strongly influences sulfur solubility in magmas. At low oxygen fugacites, magmatic sulfur exists principally as sulfide (S^{2-}) which has a relatively low solubility in silicate melts (Carroll and Rutherford 1985, 1988). Crystallization under such conditions can lead to early

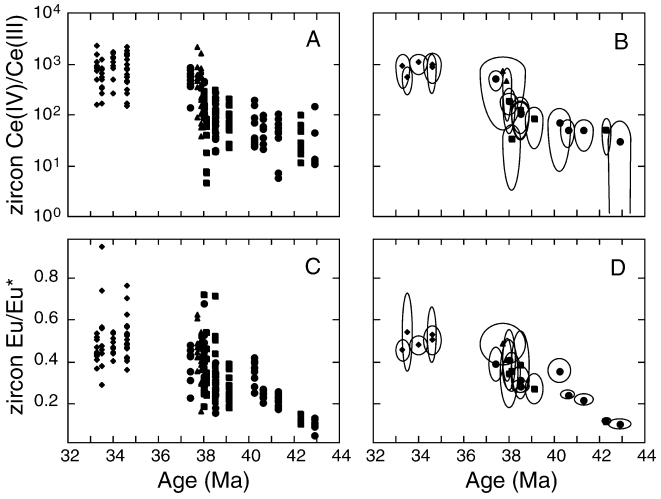

Fig. 8A–D Individual grain (**A**, **C**) and average (**B**, **D**) zircon Ce(IV)/Ce(III) and Eu_N/Eu_N* ratios plotted versus zircon U–Pb age for intrusions of the Chuquicamata-El Abra porphyry copper belt (Ballard et al. 2001, 2003). The Pajonal-El Abra intrusive suite is indicated by *circles*, the Los Picos-Fortuna suite by *squares*, the Chuquicamata Intrusive Complex (including the East, West, and Bench porphyries in the Chuquicamata mine and the major and minor facies porphyries of the Radomiro Tomic mine) by *diamonds*, and other units by *triangles*. Uncertainty envelopes are 2 standard errors for ages, and 1 standard deviation for Ce(IV)/Ce(III) and Eu_N/Eu_N* ratios. Values of zircon Ce(IV)/Ce(III) = 300 and Eu_N/Eu_N* = 0.4 effectively distinguish the ore-bearing and barren units examined in this study

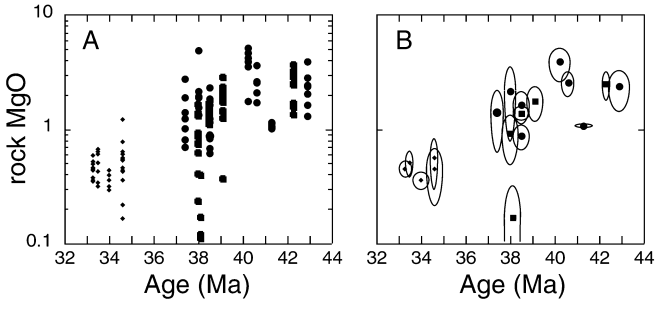

Fig. 9 Individual sample (**A**) and unit average (**B**) whole-rock MgO values (wt%) plotted versus zircon U–Pb age for intrusions of the Chuquicamata-El Abra porphyry copper belt (Ballard et al. 2001, 2003). The Pajonal-El Abra igneous suite is indicated by *circles*, the Los Picos-Fortuna suite by *squares*, the Chuquicamata Intrusive Complex (including the East, West, and Bench porphyries in the Chuquicamata mine and the major and minor facies porphyries of the Radomiro Tomic mine) by *diamonds*. Uncertainty envelopes are 2 standard errors for ages, and 1 standard deviation for MgO values. Successive intrusions of the Los Picos-Fortuna/Pajonal-El Abra complex display significant compositional overlap but unit average MgO values decrease with age

saturation of a separate sulfide phase. Chalcophile elements such as Cu and Au partition strongly into magmatic sulfide phases, in contrast to their general incompatible behavior in silicate and oxide minerals (Lynton et al. 1993; Fleet et al. 1996; Jugo et al., 1999). If a magma experiences early sulfide saturation, most of the Cu and Au will be sequestered in sulfides trapped in

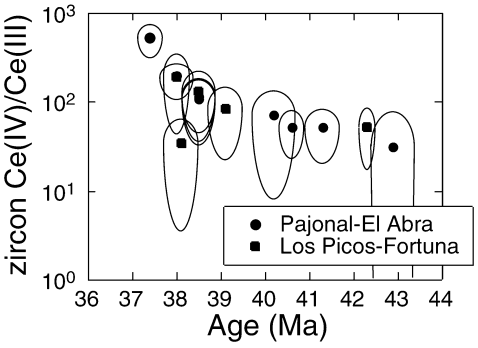

Fig. 10 Average zircon Ce(IV)/Ce(III) ratios increase systematically from the oldest, most mafic, barren intrusions of the Los Picos-Fortuna/Pajonal-El Abra igneous complex to the youngest, most felsic, and ore-bearing unit, the El Abra mine porphyry. The one apparent outlier to this trend is the Fortuna leucocratic intrusion which also displays trace-element evidence which distinguishes it from the main sequence. Zircon U–Pb ages are taken from Ballard et al. (2003)

cumulates where they will be unavailable to a late-stage magmatic-hydrothermal fluid.

At higher oxygen fugacities, magmatic sulfur exists mainly as sulfate (SO_4^{2-}) which has a much higher solubility in silicate melts than sulfide (Carroll and Rutherford 1985) and will tend to delay or even prevent saturation of a magmatic sulfide phase. The transition between sulfide-dominant and sulfate-dominant melt compositions is quite abrupt, occurring over about one log unit of oxygen fugacity (Matthews et al. 1999). Copper and Au will accumulate in the melt during differentiation under oxidized conditions, and partition into a magmatic-hydrothermal fluid should the magma reach fluid saturation (Ulrich et al. 1999). If S saturation is reached, it will involve anhydrite ($CaSO_4$) into which the chalcophile elements do not partition. Thus, all other factors being equal, oxidized sulfate-bearing hydrous magmas will contain higher concentrations of Cu, Au, and S when they exsolve a late-stage fluid phase compared to their more reduced, sulfide-saturated counterparts. As a consequence, these magmas will release magmatic-hydrothermal fluids with higher concentrations of Cu, Au, and S which, given appropriate depositional conditions, may be better able to generate Cu ± Au mineralization (Cline and Bodnar 1991; Pasteris 1996).

The seven intrusions directly associated with porphyry copper deposits are the most oxidized units of those examined here on the basis of both their individual grain and average zircon Ce(IV)/Ce(III) and Eu_N/Eu_N* ratios (Fig. 11). This correlation provides strong support for the hypothesis that oxidation state is a key factor in determining the potential of calc-alkaline magmas for forming Cu mineralization. If the explanation for the correlation involves redox-related speciation of sulfur as described above, it implies that these ore-bearing intrusions approached or passed through the sulfate–sulfide transition at least in the latter stages of their differentiation history. Conversely, the barren intrusions,

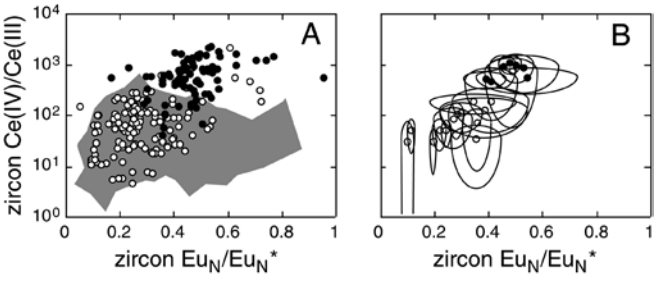

Fig. 11 Individual grain (**A**) and average (**B**) Ce(IV)/Ce(III) and Eu_N/Eu_N^* ratios in zircons from intrusions of the Chuquicamata-El Abra porphyry copper belt, illustrating the positive correlation between these two indicators of oxidation state. Data for ore-bearing intrusions are shown as *closed circles*, and for barren units as *open circles*. The patterned *field* in **A** is occupied by unpublished data for 436 detrital zircons from Paleozoic sandstones in eastern North America which support the interpretation of zircon Ce(IV)/Ce(III) and Eu_N/Eu_N^* ratios above 300 and 0.4, respectively, representing anomalous magma oxidation states

although becoming increasingly oxidized, apparently remained in the field of sulfide dominance throughout their magmatic evolution.

Implications for mineral exploration

This study has shown that seven calc-alkaline intrusions directly associated with porphyry copper mineralization have higher zircon Ce(IV)/Ce(III) ratios than 14 related but barren intrusions. This result implies that the ore-bearing porphyries were more oxidized than their barren counterparts. If these results are confirmed by further work, then the measurement of the Ce(IV)/Ce(III) ratio in zircon may provide a useful tool in exploration for porphyry copper deposits. This method has two applications. First, to discriminate between ore-bearing and barren intrusions at an early stage of exploration. Second, by measuring the Ce(IV)/Ce(III) ratio in detrital zircons from stream sediments, it should be possible to trace anomalously oxidized zircons back to their prospective igneous source.

Acknowledgement We would like to acknowledge the Chuquicamata, Radomiro Tomic, and Calama Exploraciones divisions of CODELCO, and the El Abra division of Phelps-Dodge for their logistic and technical support for this work. In particular, we would like to thank Alejandro Faunes, Roberto Fréraut, Felipe Rosas, Ruben Rardo, Patricio Cuadra, Aldo Moraga and Andres Molina for their indispensable contributions to our fieldwork. At the RSES, we thank Charlotte Allen for overseeing the smooth running of the laser-ICP-MS laboratory and for helpful discussions. Two anonymous reviewers provided useful comments on a earlier version of the paper. JRB acknowledges the support of an A.E. Ringwood scholarship from the RSES.

References

Ague JJ, Brimhall GH (1988) Magmatic arc asymmetry and distribution of anomalous plutonic belts in the batholiths of California: effects of assimilation, crustal thickness, and depth of crystallization. Geol Soc Am Bull 100(6):912–927

Allen CM, Williams IS, Stephens CJ, Fielding CR (1998) Granite genesis and basin formation in an extensional setting: the magmatic history of the northernmost New England Orogen. Aust J Earth Sci 45:875–888

Ambrus J (1977) Geology of the El Abra porphyry copper deposit, Chile. Econ Geol 72:1062–1085

Anderson DJ, Lindsley DH, Davidson PM (1993) QUILF: a PASCAL program to assess equilibria among Fe-Mg-Mn-Ti oxides, pyroxenes, olivine, and quartz. Comput Geosci 19:1333–1350

Aracena I (1981) Geologia y alteracion del sector norte del yacimiento de Chuquicamata, Taller de Titulo II. Universidad de Chile Monogr

Bacon CR, Druitt TH (1988) Compositional evolution of the zoned calc-alkaline magma chamber of Mount Mazama, Crater Lake, Oregon. Contrib Mineral Petrol 98:224–256

Ballard JR, Palin JM, Williams IS, Campbell IH, Faunes A (2001) Two ages of porphyry intrusion resolved for the super-giant Chuquicamata copper deposit of northern Chile by ELA-ICP-MS and SHRIMP. Geology 29(5):383–386

Ballard JR, Palin JM, Campbell IH, Faunes A (2003) In situ zircon U-Pb geochronology of the Chuquicamata, Fortuna and El Abra magmatic complexes of northern Chile. Econ Geol (in press)

Blevin PL, Chappell BW (1992) The role of magma sources, oxidation states and fractionation in determining the granite metallogeny of eastern Australia. Trans R Soc Edinb Earth Sci 83:305–316

Blundy J, Wood B (1994) Prediction of crystal-melt partition coefficients from elastic moduli. Nature 372:452–454

Boric PR, Diaz FF, Maksaev JV (1990) Regional map (1987), scale 1:500,000. Geologia y yacimientos metaliferos de la region de Antofagasta. Serv Nacl Geol Mineria 40

Candela PA (1986) The evolution of vapor from silicate melt: effect on oxygen fugacity. Geochim Cosmochim Acta 50:1205–1211

Candela PA (1992) Controls on ore metal ratios in granite-related ore systems: an experimental and computational approach. Trans R Soc Edinb Earth Sci 83:317–326

Carmichael ISE, Ghiorso MS (1986) Oxidation-reduction relations in basic magma: a case for homogeneous equilibria. Earth Planet Sci Lett 78:200–210

Carroll MR, Rutherford MJ (1985) Sulfide and sulfate saturation in hydrous silicate melts. In: Proc 15th Lunar and Planetary Science Conf, part 2. J Geophys Res Suppl 90:C601–C612

Carroll MR, Rutherford MJ (1988) Sulfur speciation in hydrous experimental glasses of varying oxidation state: results from measured wavelength shifts of sulfur X-rays. Am Mineral 73:845–849

Cherniak DJ, Hanchar JM, Watson EB (1997) Rare-earth diffusion in zircon. Chem Geol 134:289–301

Chong G, Pardo RC (1994) Map, scale 1:100 000, Chuquicamata District. Corporacion Nacional del Cobre de Chile, Gerencia de Exploraciones, Calama

Cline JS, Bodnar RJ (1991) Can economic porphyry copper mineralization be generated by a typical calc-alkaline melt? J Geophys Res 96:8113–8126

Cuadra P, Zentilli M, Puig A, Tidy E (1997) Dataciones radiometricas en Radomiro Tomic. In: 8th Congr Geológico Chileno, vol 3, pp 1899–1902

Czamanske GK, Wones DR (1973) Oxidation during magmatic differentiation, Finnmarka complex, Oslo area, Norway. Part 2. The mafic silicates. J Petrol 14:349–380

Dilles JH, Tomlinson AJ, Martin MW, Blanco N (1997) El Abra and Fortuna Complexes: A porphyry copper batholith sinistrally displaced by the Falla Oeste. In: 8th Congr Geológico Chileno, vol 3, pp 1883–1887

Drake MJ (1975) The oxidation state of europium as an indicator of oxygen fugacity. Geochim Cosmochim Acta 39:55–64

Duncan RA, Hargraves RB (1984) Plate evolution of the Caribbean region in the mantle reference frame: The

Caribbean-South American plate boundary and regional tectonics. Geol Soc Am Mem 162:81–93
Dunn T, Sen C (1994) Mineral/matrix partition coefficients for orthopyroxene, plagioclase, and olivine in basaltic to andesitic systems: A combined analytical and experimental study. Geochim Cosmochim Acta 58(2):717–733
Eggins SM, Rudnick RL, McDonough WF (1998) The composition of peridotites and their minerals: a laser-ablation ICP-MS study. Earth Planet Sci Lett 154:53–71
Fleet ME, Crocket JH, Stone WE (1996) Partitioning of platinum-group elements (Os, Ir, Ru, Pt, Pd) and gold between sulfide liquid and basalt melt. Geochim Cosmochim Acta 60:2397–2412
Ghaderi M, Palin JM, Campbell IH, Sylvester PJ (1999) Rare earth element systematics in scheelite from hydrothermal gold deposits in the Kalgoorlie-Norseman region, Western Australia. Econ Geol 94(3):423–437
Graichen RE, Dean DA, Barrett LF, Burton WD, Christensen DK (1995) Geologic overview of the El Abra porphyry copper deposit, Chile. Cyprus Amax Minerals Company Internal Rep, El Abra, pp 1–11
Hanchar JM, Finch RJ, Hoskin PWO, Watson EB, Cherniak DJ, Mariano AN (2001) Rare earth elements in synthetic zircon. 1. Synthesis, and rare earth element and phosphorous doping. Am Mineral 86:667–680
Hedenquist JW, Lowenstern JB (1994) The role of magmas in the formation of hydrothermal ore deposits. Nature 370:519–527
Hinton RW, Upton BGJ (1991) The chemistry of zircon: Variations within and between large crystals from syenite and alkali basalt xenoliths. Geochim Cosmochim Acta 55:3287–3302
Jugo PJ, Candela PA, Piccoli PM (1999) Magmatic sulfides and Au:Cu ratios in porphyry deposits: an experimental study of copper and gold partitioning at 850 °C, 100 MPa in a haplogranitic melt-pyrrhotite-intermediate solid solution-gold metal assemblage, at gas saturation. Lithos 46:573–589
Klein M, Stosch H-G, Seck HA, Shimizu N (2000) Experimental partitioning of high field strength and rare earth elements between clinoyroxene and garnet in andesitic to tonalitic systems. Geochim Cosmochim Acta 64(1):99–115
Lindsay D, Zentilli M, Rojas de la Rivera J (1995) Evolution of an active ductile to brittle shear system controlling mineralization at the Chuquicamata porphyry copper deposit, northern Chile. Int Geol Rev 37:945–958
Loucks RR, Eggins SM, Shelly JMG, Kinsley LPJ, Ware NJ (1995) Development of the inductively-coupled-plasma mass-spectrometry ultraviolet laser trace-element micro-analyser (ICPMS-ULTEMA). 1995 Annu Rep Research School of Earth Sciences, Australian National University, Canberra, pp 138–140
Lynton SJ, Candela PA, Piccoli PM (1993) An experimental study of the partitioning of copper between pyrrhotite and a high silica rhyolite melt. Econ Geol 88:901–915
Maksaev J, Tomlinson AJ (1995) Cuadrangulo Cerros de Paqui, Region de Antofagasta, map, scale 1:50,000. Servicio Nacional de Geologia y Mineria y Corporacion Nacional del Cobre Informe Registrado IR-95-07
Maksaev J, Tomlinson AJ, Blanco NP (1994) Estudio geologico de la franja longitudinal comprendida entre Quebrada Blanca y Chuquicamata. Servicio Nacional de Geologia y Mineria y Corporacion Nacional del Cobre, Propuesta para Informe Final Convenio Codelco-Sernageomin
Matthews SJ, Jones AP, Bristow CS (1992) A simple magma-mixing model for sulphur behavior in calc-alkaline volcanic rocks: mineralogic evidence from Mount Pinatubo 1991 eruption. J Geol Soc Lond 149:863–866
Matthews SJ, Moncrieff DHS, Carroll MR (1999) Empirical calibration of the sulphur valence oxygen barometer from natural and experimental glasses: method and applications. Mineral Mag 63(3):421–431
McInnes BIA, Cameron EM (1994) Carbonated, alkaline hybridizing melts from the sub-arc enviroment: mantle wedge samples from the Tabar-Lihir-Tanga-Feni arc, Papua New Guinea. Earth Planet Sci Lett 122:125–141
McInnes BIA, Farley KA, Sillitoe RH, Kohn BP (1999) Application of apatite (U-Th)/He thermochronometry to the determination of the sense and amount of vertical displacement at the Chuquicamata porphyry copper deposit, Chile. Econ Geol 94:937–948
Nash WP, Crecraft HR (1985) Partition coefficients for trace elements in silicic magmas. Geochim Cosmochim Acta 49:2309–2322
Onuma N, Higuichi H, Wakita H, Nagasawa H (1968) Trace element partitioning between two pyroxenes and the host lava. Earth Planet Sci Lett 5:47–51
Ossandón C, Zentilli M (1997) El Distrito de Chuquicamata: una concentraction de cobre de clase mundial. In: 8th Congr Geológico Chileno, vol 3, pp 1888–1893
Pallister JS, Hoblitt RP, Reyes AG (1992) A basalt trigger for the 1991 eruption of Pinatubo Volcano? Nature 356:426–428
Pardo RC, Rivera SC (1999) Exploracion basica de seguimiento distrito Chuquicamata II Region, Informe de Resultados. Calama Exploraciones, Corporacion Nacional del Cobre de Chile Rep API-9701-3, pp 35–39
Pasteris JD (1996) Mount Pinatubo volcano and "negative" porphyry copper deposits. Geology 24(12):1075–1078
Pearce NJG, Perkins WT, Westgate JA, Gorton MP, Jackson SE, Neal CR, Chenery SP (1997) A compilation of new and published major and trace element data for NIST SRM 610 and NIST SRM 612 glass reference materials. Geostand Newsl 21(1):115–144
Philpotts JA (1970) Redox estimation from a calculation of Eu^{2+} and Eu^{3+} concentration in natural phases. Earth Planet Sci Lett 9:257–268
Reutter K-J, Scheuber E, Chong G (1996) The Precordilleran fault system of Chuquicamata, northern Chile: evidence for reversals along arc-parallel strike-slip faults. Tectonophysics 259:213–228
Reynolds P, Ravenhurst C, Zentilli M, Lindsay D (1998) High-precision $^{40}Ar/^{39}Ar$ dating of two consecutive hydrothermal events in the Chuquicamata porphyry copper system, Chile. Chem Geol 148:45–60
Rosas F (1999) Geología, alteracion y mineralización del Proyecto San Lorenzo. Thesis, Universidad de Chile, Santiago
Sillitoe RH (1992) Gold and copper metallogeny of the central Andes – past, present and future exploration objectives. SEG distinguished lecture. Econ Geol 87:2205–2216
Sillitoe RH, Marquardt JC, Ramírez F, Becerra H, Gómez M (1996) Geology of the concealed MM porphyry copper deposit, Chuquicamata district, northern Chile. In: Camus F et al. (eds) Andean copper deposits: new discoveries, mineralization, styles and metallogeny. Soc Econ Geol Spec Publ 5:59–70
Tomlinson AJ, Maksaev J, Blanco N (1995) Cuadrangulo Cerro Jaspe, Region de Antofagasta, map, scale 1:50,000. Servicio Nacional de Geologia y Mineria y Corporacion Nacional del Cobre Informe Registrado IR-95-07
Ulrich T, Günther D, Heinrich CA (1999) Gold concentrations of magmatic brines and the metal budget of porphyry copper deposits. Nature 399:676–679
Wilke M, Behrens H (1999) The dependence of the partitioning of iron and europium between plagioclase and hydrous tonalitic melt on oxygen fugacity. Contrib Mineral Petrol 137: 102–114
Williams S (1997) Anexo XI Informe Petrografico. Calama Exploraciones, Corporacion Nacional del Cobre de Chile Rep COBRE01/97
Zentilli M, Graves MC, Lindsay D (1994) Mineralogical, geochemical and structural study of Chuquicamata. Rep Corporacion Nacional del Cobre de Chile, Chuquicamata